University of Nebraska - Lincoln
DigitalCommons@University of Nebraska - Lincoln

Peter Dowben Publications Research Papers in Physics and Astronomy

2022

What happens when transition metal trichalcogenides are interfaced with gold?

Archit Dhingra

Dmitri E. Nikonov

Alexey Lipatov

Alexander Sinitskii

Peter Dowben

Follow this and additional works at: https://digitalcommons.unl.edu/physicsdowben

Part of the Atomic, Molecular and Optical Physics Commons, Condensed Matter Physics Commons, Engineering Physics Commons, and the Other Physics Commons

This Article is brought to you for free and open access by the Research Papers in Physics and Astronomy at DigitalCommons@University of Nebraska - Lincoln. It has been accepted for inclusion in Peter Dowben Publications by an authorized administrator of DigitalCommons@University of Nebraska - Lincoln.

Journal of MATERIALS RESEARCH

Invited Feature Paper-Review
DOI:10.1557/s43578-022-00744-6

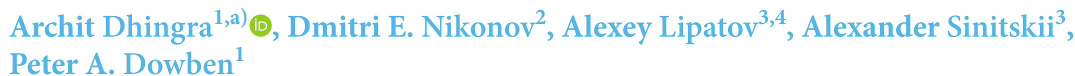

EARLY CAREER SCHOLARS IN MATERIALS SCIENCE 2023

ANNUAL ISSUE

What happens when transition metal trichalcogenides are interfaced with gold?

Archit Dhingra[1,a)], Dmitri E. Nikonov[2], Alexey Lipatov[3,4], Alexander Sinitskii[3], Peter A. Dowben[1]

[1] Department of Physics and Astronomy, University of Nebraska–Lincoln, 855 North 16th Street, Lincoln, NE 68588-0299, USA
[2] Components Research, Intel Corporation, Hillsboro, OR 97124, USA
[3] Department of Chemistry, University of Nebraska–Lincoln, 639 North 12th Street, Lincoln, NE 68588-0304, USA
[4] Department of Chemistry, Biology & Health Sciences and Karen M. Swindler Department of Chemical and Biological Engineering, 501 E. Saint Joseph Street, South Dakota School of Mines and Technology, Rapid City, SD 57701, USA
[a)] Address all correspondence to this author. e-mail: archit.dhingra@huskers.unl.edu

Received: 29 June 2022; accepted: 13 September 2022

Transition metal trichalcogenides (TMTs) are two-dimensional (2D) systems with quasi-one-dimensional (quasi-1D) chains. These 2D materials are less susceptible to undesirable edge defects, which enhances their promise for low-dimensional optical and electronic device applications. However, so far, the performance of 2D devices based on TMTs has been hampered by contact-related issues. Therefore, in this review, a diligent effort has been made to both elucidate and summarize the interfacial interactions between gold and various TMTs, namely, In_4Se_3, TiS_3, ZrS_3, HfS_3, and $HfSe_3$. X-ray photoemission spectroscopy data, supported by the results of electrical transport measurements, provide insights into the nature of interactions at the Au/In_4Se_3, Au/TiS_3, Au/ZrS_3, Au/HfS_3, and Au/$HfSe_3$ interfaces. This may help identify and pave a path toward resolving the contemporary contact-related problems that have plagued the performance of TMT-based nanodevices.

Archit Dhingra

Archit Dhingra Dr. Archit Dhingra received his bachelor's degree in Engineering Physics from DelhiTechnological University in 2017. In 2021, he was awarded his PhD in Physics & Astronomyfrom the University of Nebraska-Lincoln under the supervision of Prof. Peter A. Dowben. Uponcompletion of his PhD, he continued working with his doctoral advisor as a postdoctoralresearcher until June 2022. He is currently a member of "Ramon y Cajal Researcher," Dr.Alejandro Molina Sanchez's group at the Instituto de Ciencia de Materiales Universidad deValencia (ICMUV). Dhingra's research interests include experimental characterization of the electronic structure of2D van der Waals materials and strongly correlated oxides using various photoemissionspectroscopy techniques. In particular, he is focused on understanding the physical and electronicproperties of low-dimensional materials and their heterostructures for possible applications inspintronics and nano-optoelectronic devices.

Introduction

Shrinkage of the lengths and widths of transistor channels down to a few nanometers does not favor the use of three-dimensional semiconductor materials as transistor channels for field-effect transistors (FET). So is the case because, in the nano regime, the gate oxide cannot offer reliable control of the channel bias owing to the drain-induced barrier lowering (DIBL) [1–4]. DIBL induces a short-channel effect [2–4], which increases the leakage current causing undesirable power dissipation even when the device is turned off [5]. Mathematically, the potential distribution in a transistor channel is roughly described by Poisson's equation, which is partly addressed by introducing a natural

© The Author(s) 2022

length scale $\mu = \sqrt{t_s t_d (\frac{\mathcal{E}_s}{\epsilon_d})}$, where t_s is the thickness of the semiconductor channel, t_b is the thickness of the gate oxide, and $\mathcal{E}_s$ and $\mathcal{E}_d$ are the dielectric constants of the semiconductor and gate oxide, respectively [6–8]. This natural length scale (μ) indicates how efficiently the gate and gate dielectric control the channel. As a rough metric, for highly efficient control, the semiconductor conduction channel should be at least five times smaller than the length of the channel [5]. Thus, for efficient device performances, the shorter the semiconductor channel, the thinner it must be. Consequently, to circumvent the deleterious short-channel effects, two-dimensional (2D) semiconducting materials are thought to be favored as the transistor channels. This solution to combat the short-channel effects will, however, only work if these 2D semiconducting materials are not plagued by the catastrophic edge scattering or edge states that make the semiconductor channel metallic.

2D semiconducting transition metal trichalcogenides (TMTs), with quasi-one-dimensional (quasi-1D) chains [9–17], are among the few 2D systems with suppressed unwanted edge disorders that have afflicted some well-studied 2D materials like graphene [18, 19], its derivatives [20], and the transition metal dichalcogenides [21–26]. Their quasi-1D structure helps combat detrimental edge scattering and unfavorable edge states, which have detrimental effects on the performance of nanodevices as the transistor channel widths shrink to 10 nm or less [18, 27–32]. This makes the TMTs attractive for a plethora of low-dimensional device applications [33–46]. Owing to their low-symmetry [47–51], the TMTs are also great for highly anisotropic optoelectronic applications [43–45, 52–56]. That said, as is the case with all solid-state devices, contact issues abound [57–59] and can potentially diminish device performance significantly, so the interface between the metal contacts and TMTs must be investigated extensively. Such investigations are especially important in the case of TMTs since their band alignments have been shown to be quite complex [60].

The purpose of this concise yet comprehensive review is to encapsulate recent research efforts that are all targeted toward deciphering the metal–TMT interface and provide an outlook for further technological development in the field of TMT-based devices. This work focuses on the interface resulting from the interactions between TMTs and Au, since it is one of the most commonly used materials for making connections and contacts to commercial semiconductors [61, 62]. Au, a metal with a very high work function [63–65], is frequently regarded as a chemically inert metal in comparison with most metals but chemical reactions with Au are still possible. Since this review is focused on the surface and metal contact interfaces of the semiconducting TMTs, the emphasis here is on the TMTs studied thoroughly enough such that their reported device characteristics are backed by systematic X-ray photoemission spectroscopy (XPS) measurements. Prior review articles (see refs. [39, 40]) have not addressed the very important metal–TMT interface, but given the increasing attention given to TMT devices, discussion of the interfacial interactions between Au and each of the following TMTs, In_4Se_3, TiS_3, ZrS_3, HfS_3, and $HfSe_3$, is both timely and of importance.

Experimental details

The In_4Se_3 single crystals were synthesized via the Czochralski method in a graphite-based crucible, in the presence of hydrogen, at 540°C [50, 53, 66]. The studied TiS_3 crystals were synthesized through a direct reaction between sulfur vapors and metallic titanium in vacuum-sealed quartz ampules, which were heated at 550°C, as has been reported in prior works [13, 67–69]. Likewise, the ZrS_3 crystals were obtained as the product of a chemical reaction between vapors of sulfur and metallic zirconium, in vacuum-sealed quartz ampules at 800°C [69–71]. For the synthesis of HfS_3 crystals, just like its titanium and zirconium counterparts, metallic hafnium was made to react with sulfur vapors in a vacuum-sealed quartz ampule at 600°C [72, 73]. Eventually, after annealing the HfS_3 ampules at 600°C for 2 weeks [72, 73], a few-millimeter long crystals of HfS_3 were gathered. The $HfSe_3$ crystals were synthesized from elemental hafnium and selenium as described in the following text. About 0.2 g of hafnium foil (Alfa Aesar, 99.9% metal basis excluding Zr, Zr nominal 2%) and 0.3 g of selenium powder (~ 13% excess to stoichiometry; Alfa Aesar, 325 mesh, 99.999%) were sealed in a quartz ampule under a vacuum of about 200 mTorr. The ampule was placed in a tube furnace with one side of the ampule located near the edge of the furnace to create a temperature gradient. The furnace was heated to 750°C and the ampule was annealed for the duration of 7 days, after which the furnace was slowly cooled down. The excess of selenium accumulated at the colder end of the ampule, while 2-mm-long black $HfSe_3$ crystals were found on hafnium foil and on the inside of the quartz tube.

The XPS spectra of TiS_3, ZrS_3, and HfS_3 were collected using an Al K_α SPECS X-ray anode, with the X-ray photon energy of 1486.6 eV, and a PHI hemispherical electron analyzer (Model: 10-360). All the XPS measurements were carried out in an ultra-high vacuum chamber as the base pressure was always better than 1.9×10^{-10} Torr, as described elsewhere [73–75]. To extract the information about the individual S 2p core-level components, the fits to all the XPS spectra were performed using the XPST curve fitting package available in Igor Pro.

The Au coverage-dependent XPS spectra of $HfSe_3$ crystals were recorded using the same equipment and under similar parameters as mentioned above. Deposition of Au adlayers onto the surface of $HfSe_3$ crystals was achieved by thermal evaporation using a tungsten wire basket, and the thickness of the

© The Author(s) 2022

thermally evaporated Au adlayers ascertained with the help of a thickness monitor, as described elsewhere [75].

Surfaces of the TMTs

Knowledge of the correct crystal structure and surface termination of a material is indispensable if its device properties are to be properly investigated and understood. This is because the surface of a material and the interactions occurring at the interface, between the material and the metal contact, have strong influence on device characteristics of a material [76–78]. The TMTs that are subject of this work, especially the MS_3-type, have been much investigated recently. It is not just the sheer variety of their promising applications [12, 33, 34, 39–42] that makes them exciting, but also the abundance of exotic physics they possess [16, 37]. However, as is the case for any material, both the fundamental understanding of these TMTs and a reliable realization of their device applications rely heavily on the correct interpretation of the information conveyed by standard characterization techniques. This problem has often been addressed by combining device characterization with photoemission spectroscopy studies, which is now a decades-long tradition.

Surface termination of materials can easily be determined through angle-resolved X-ray photoemission spectroscopy (angle-resolved XPS). This is a technique that is known to offer nondestructive depth-profiling of materials [79]. As angle-resolved XPS is an enhancement of the usual XPS technique, its results provide information that can be even more surface sensitive [80] in nature than the information collected by the standard normal-emission XPS [81]. The basic mathematical equation describing the working principle of this technique, i.e., angle-resolved XPS, is the well-known Beer–Lambert law equation [79, 82]. The Beer–Lambert law equation can be derived from the scratch with a trivial assumption. The assumption is that upon traveling an infinitesimal distance *ds* through a continuum the photoelectron flux intensity *I* is attenuated by *dI*, which is proportional to both the distance traveled through the continuum and the flux intensity (i.e., $dI = -IAds$) [79]. However, without diving deep into the mathematical treatment of the Beer–Lambert law, the equation applicable to the angle-resolved XPS data collected for real samples (as opposed to a theoretically assumed continuum) is given as [79, 82]:

$$I = I_0 e^{\left(\frac{-z}{\lambda \cos\theta}\right)}.$$

In this equation, *I* is the attenuated photoelectron flux intensity that is received at the photoelectron detector from a layer of atoms located at a vertical probing depth *z* beneath the surface of the material. Here, I_0 is the photoelectron flux intensity that is received at the detector from a layer of atoms at the surface of the material, and θ is the photoemission take-off angle with respect to the normal to the surface of the sample. The remaining parameter in the above equation, λ, is the inelastic mean free path of the detected photoelectron [83–85]. As the name suggests, the inelastic mean free path of a photoelectron signifies how far it can travel on average before losing its energy as a consequence of inelastic collisions. Therefore, the inelastic mean free path of a photoelectron quantifies its attenuation length as it travels within the sample [79, 83–85]. Moreover, since plasmonic excitations are responsible for most of the energy losses that occur in photoemission spectroscopy, the inelastic electron mean free path tends to be shorter for metals than it is for either semiconductors or dielectrics. Just the same, the mean free path of the typical photoelectron generated with an Al K_α or Mg K_α X-ray source is typically 1 to 2 nm or less, which is to say that the XPS probing depth will be very short and limited to the surface region of the studied TMTs.

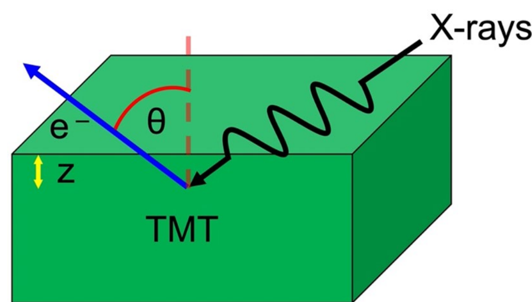

Figure 1: A schematic representation of the geometry of an angle-resolved XPS measurement.

An extensive derivation of the Beer–Lambert law equation and a detailed description of the all the parameters, which appear in this equation, are presented in ref. [79]. A schematic representation of the geometry of an angle-resolved XPS measurement is shown in Fig. 1. In Fig. 1, the X-rays incident on the TMT samples (in green) are shown in black, while the emitted photoelectron is depicted by the arrow in blue. The vertical probing depth *z* beneath the surface of the TMT is illustrated by the double-sided arrow (in yellow), and the photoemission take-off angle θ, with respect to the normal to the surface of the studied TMT, is signified by the red arc. While a little cumbersome, angle-resolved XPS may also be used to calculate the thickness of the samples of interest [79, 80, 82], if the layers are thin enough (i.e., on the nanometer scale).

Single-phase In_4Se_3 tends to crystallize in the orthorhombic *Pnnm* space group [48, 86] with four formula units per cell ($Z = 4$) with the lattice constants *a*, *b*, and *c* equal to 1.2355 nm, 1.5350 nm, and 0.4097 nm, respectively [48, 53]. The representative crystal structure of In_4Se_3, with quasi-2D clusters of $[(In_3)^{5+}(Se^{2-})_3]^-$ and 1D chains [53, 75, 87], is shown in Fig. 2(a). Despite its layered structure, In_4Se_3 is not a van der Waals (vdW) material due to the highly ionic nature of the interlayer interactions [53]. Based on the angle-resolved XPS measurements

© The Author(s) 2022

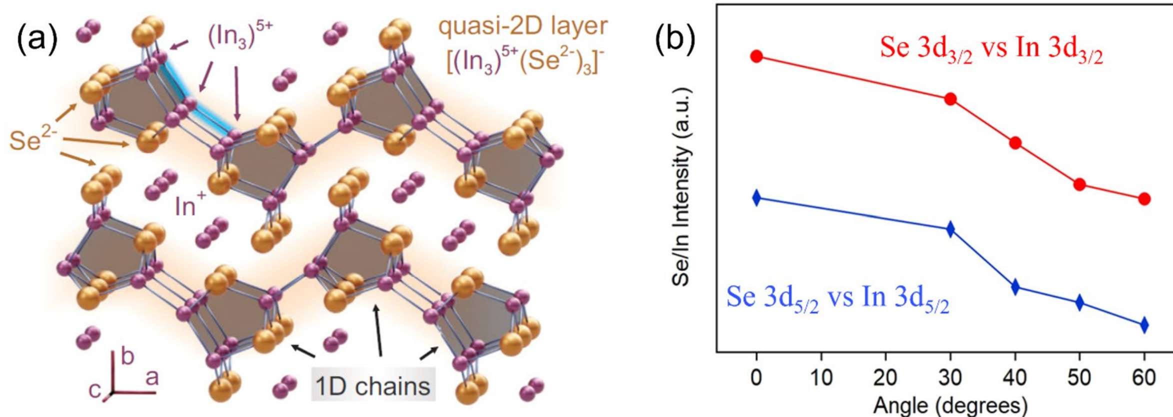

Figure 2: (a) The crystal structure of In_4Se_3. Reprinted figure with permission from ref. [53]. Copyright (2021) by Wiley. (b) Angle-resolved XPS intensity ratio of the Se 3d core-level to In 3d core-level [75]. © IOP Publishing. Reproduced with permission. All rights reserved.

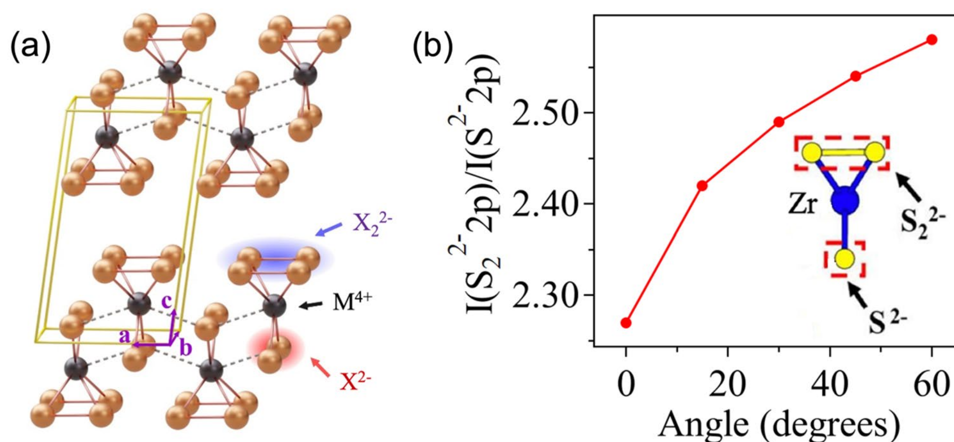

Figure 3: (a) The crystal structure of the MX_3-type TMTs and (b) angle-resolved photoemission intensity ratio of the S_2^{2-} 2p core-level to the S^{2-} 2p core-level of ZrS_3 [90]. © IOP Publishing. Reproduced with permission. All rights reserved.

[shown in Fig. 2(b)], the surface of In_4Se_3, contrary to the theoretical predictions, is found to terminate in indium [75]. It is also worth mentioning that indium from the bulk of In_4Se_3 tends to segregate to the selvedge (or subsurface region) as the sample temperature is increased [88], suggesting that region near the surface of In_4Se_3 is likely to become rich in indium. The indium-rich surface region could be an important factor to consider from the standpoint of device fabrication as the indium-rich surface may affect the contact potential.

Unlike In_4Se_3, all the other TMTs that are discussed here, i.e., TiS_3, ZrS_3, HfS_3, and $HfSe_3$, are more akin to vdW materials [13] and bear the MX_3 (M = transition metal; X = chalcogen) form. While the lattice constants of all these MX_3-type TMTs differ, they do belong to the same space group and are isostructural [52, 69, 89]. Figure 3(a) shows the crystal structure of an MX_3-type TMT where X^{2-} and X_2^{2-} indicate two distinct chalcogen species; since all the MX_3-type TMTs are isostructural, determining the surface termination of just one of them would suffice as it would be the same for all other TMTs of the MX_3 kind. Figure 3(b) shows results of the angle-resolved XPS of ZrS_3, which implies that the surface of ZrS_3 terminates in disulfide (S_2^{2-}) and not sulfide (S^{2-}) [90]. Because the MX_3-type TMTs are isostructural, the insights into the surface termination of ZrS_3 can be extended to all other MX_3-type TMTs. In other words, TiS_3 and HfS_3 should also terminate in disulfide and $HfSe_3$ should terminate in diselenide (Se_2^{2-}).

While isostructural with TiS_3 and ZrS_3, unlike TiS_3 and ZrS_3, the photoemission spectroscopy data of HfS_3 show signature of oxidation of hafnium that appears to occur upon exposure of HfS_3 to ambient air [73], implying that the surface of HfS_3 is nontrivial. Figure 4 shows the XPS data of the Hf 4f core-level of HfS_3. The red triangles in Fig. 4 represent the raw photoemission spectrum of the Hf 4f core-level and the fits are indicated by the solid lines. The overall fit to the raw data (solid black

© The Author(s) 2022

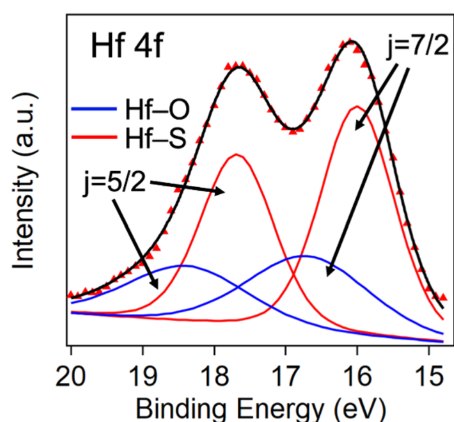

Figure 4: The photoemission spectrum of the Hf 4f core-level of HfS_3. Reproduced from ref. [73] with permission from the Royal Society of Chemistry.

line) requires two Hf 4f doublets (shown by solid red and solid blue lines). The higher intensity doublet (solid red lines) consists of an Hf $4f_{7/2}$ peak at 16.0 ± 0.1 eV and an Hf $4f_{5/2}$ peak at 17.7 ± 0.1 eV, implying a spin–orbit splitting of ~ 1.7 eV between the two peaks. The lower intensity doublet, shown by solid blue lines, has the two Hf 4f peaks separated by ~ 1.7 eV as well, with the Hf $4f_{7/2}$ peak occurring at 16.7 ± 0.1 eV and the Hf $4f_{5/2}$ peak appearing at 18.4 ± 0.1 eV. The higher binding energy of the Hf 4f doublet in blue, in comparison with the binding energy value of the doublet in red, implies more charge donation in the former case compared to the latter. Therefore, in accordance with the existing literature [91–95], the lower intensity Hf 4f core-level doublet at the higher binding energy value is attributed to the Hf–O bonding environment; whereas the Hf 4f core-level doublet at the lower binding energy is characteristic of the Hf–S bonding environment [73]. These results imply facile dissociative chemisorption of oxygen on HfS_3. Now, this is crucial because the oxygen chemisorption at the surface of HfS_3 helps reconcile two prior experimental studies on HfS_3 with contradictory claims, as the study conducted by Xiong et al. [96] showed that HfS_3 is a p-type semiconducting material, whereas the study conducted by Flores et al. [97] claimed that HfS_3 is an n-type material instead. Chemisorption of oxygen at the HfS_3 is also consistent with the electrical transport data shown in refs. [73, 96], and explains how the exposure of HfS_3 to ambient air makes it transition from being an n-type semiconductor, in its as-synthesized form, to a p-type semiconductor.

While there exist several photoemission spectroscopy studies on these three TMTs (i.e., TiS_3 [36, 52, 68, 69, 74, 89], ZrS_3 [52, 69, 89, 90], and HfS_3 [73]), a comparison of the core-level photoemission data for the sulfur core-levels of each of these trichalcogenides can provide indications of predominant location of the sulfur vacancies [98, 99]. In the case of HfS_3, such a comparison can help identify the location of sulfur sites that are filled in by oxygen instead. Figure 5 shows the photoemission spectra of the S 2p core-levels of TiS_3, ZrS_3, and HfS_3. The fits to the S 2p core-level spectra of both TiS_3 [Fig. 5(a)] and ZrS_3 [Fig. 5(b)] indicate four distinctive photoemission features for each of the TMTs, where two of these features are attributed to the S^{2-} 2p core-level and the remaining two correspond to the S_2^{2-} 2p core-level. In agreement with the existing literature [69, 90], the four characteristic S 2p core-level components are observed at three different binding energies: 161.1 ± 0.1 eV (S^{2-} $2p_{3/2}$), 162.3 eV ± 0.1 eV (S^{2-} $2p_{1/2}$ and S_2^{2-} $2p_{3/2}$), and 163.5 ± 0.1 eV (S_2^{2-} $2p_{1/2}$). Similarly, not unlike in the case of TiS_3 and ZrS_3, the S 2p XPS spectrum of HfS_3 [Fig. 5(c)] envelops two S^{2-} 2p and two S_2^{2-} 2p core-level components. As recently reported [73], these four S 2p components are seen at 161 ± 0.1 eV (S^{2-} $2p_{3/2}$), 162.2 eV ± 0.1 eV

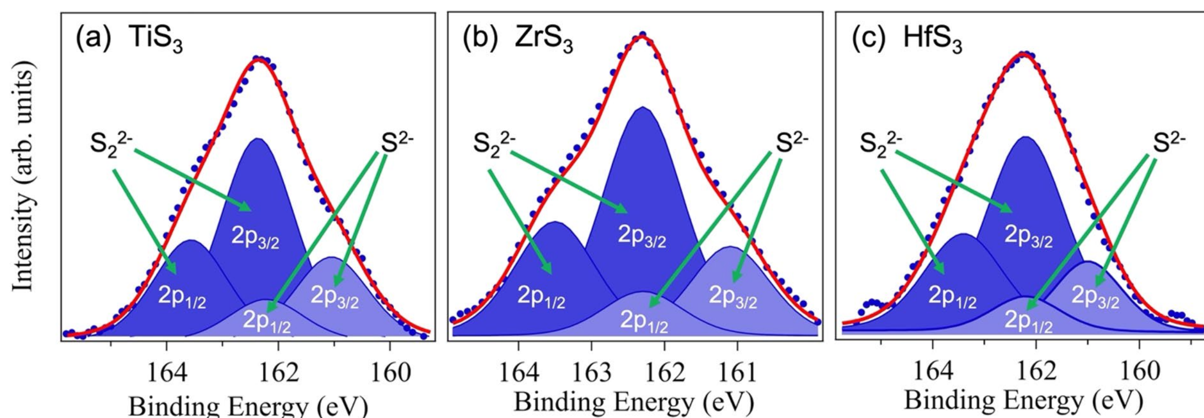

Figure 5: The XPS spectra of the S 2p core-levels of (a) TiS_3, (b) ZrS_3, and (c) HfS_3. The solid circles represent the raw data while the overall fits to the raw data are shown by the solid red lines. Each of these spectra contains four photoemission components: S^{2-} $2p_{3/2}$, S^{2-} $2p_{1/2}$, S_2^{2-} $2p_{3/2}$, and S_2^{2-} $2p_{1/2}$. All the individual S 2p core-level components are indicated by green arrows.

© The Author(s) 2022

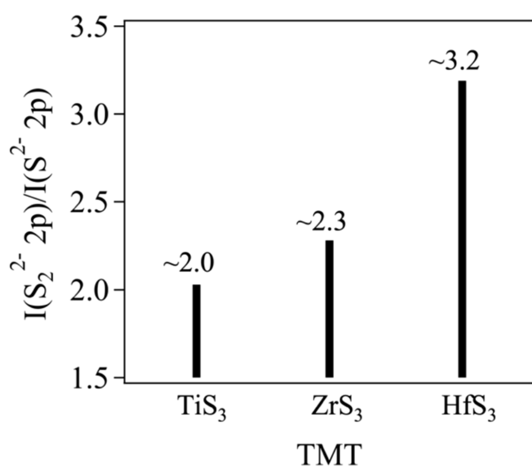

Figure 6: The ratio of the XPS peak areas of the S_2^{2-} 2p to the S^{2-} 2p, for a given TMT, as a function of the *Z* of the transition metal that both the sulfur species are bonded to. The photoemission peak areas of both the S 2p core-levels of TiS_3, ZrS_3, and HfS_3 were calculated from the XPS spectra shown in Fig. 5.

(S^{2-} $2p_{1/2}$ and S_2^{2-} $2p_{3/2}$), and 163.4 ± 0.1 eV (S_2^{2-} $2p_{1/2}$). Overall, it is fair to say that the binding energy values of the four S 2p core-level features of HfS_3 are in great agreement with the binding energy values of the four S 2p core-level components of its zirconium and titanium counterparts. This is, therefore, both expected and reassuring since all these three TMTs are isostructural [69, 73]. Nonetheless, a closer look into the XPS spectra of their respective S 2p core-levels discloses that HfS_3 differs from both TiS_3 and ZrS_3.

The variation in the ratio of the photoemission peak areas of the S_2^{2-} 2p core-level to the S^{2-} 2p core-level as a function of the *Z* of the transition metal, which both the sulfur species are bonded to, is summarized in Fig. 6. All the photoemission peak areas, used to plot Fig. 6, were calculated from the S 2p core-level XPS spectra shown in Fig. 5. From the trend shown in Fig. 6, it can be inferred that the XPS intensities of the S_2^{2-} 2p and S^{2-} 2p core-level photoelectrons depend on the transition metal they are bonded to. While this could partly be a direct consequence of a variation in the inelastic mean free path of the S 2p core-level photoelectrons, the oxidation HfS_3 is in fact the likely origin of why there is a significant increase in the $I(S_2^{2-}\ 2p)/I(S^{2-}\ 2p)$ ratio for HfS_3. The high ratio of the photoemission peak areas of the S_2^{2-} 2p core-level to the S^{2-} 2p core-level of HfS_3 is in agreement with the existing theory [11, 100] that found the S^{2-} vacancy formation to be the most energetically likely scenario among all the possible vacancy formation scenarios. The highly likely S^{2-} vacancy formation in HfS_3 along with a $I(S_2^{2-}\ 2p)/I(S^{2-}\ 2p)$ ratio of ~ 3.2 is also consistent with the chemisorption of oxygen at the HfS_3 surface and indicates that oxygen preferentially binds itself to Hf by occupying the S^{2-} vacancies.

Our analyses of the XPS spectra of the S 2p core-levels of TiS_3, ZrS_3, and HfS_3, therefore, imply that oxygen occupies the sulfur sites in HfS_3 that are the most highly coordinated with the Hf ions, i.e., the S^{2-} sites. The displacement of sulfur atoms in HfS_3 by oxygen atoms thus implies that the nature of this displacement is such that the oxygen atoms show affinity toward binding with the Hf ions via the sulfur sites that participate in stronger Hf–S bonds. Such an oxygen chemisorption mechanism ensures that once oxygen binds itself to Hf ions, more electron charge is donated by the Hf ions to the oxygen atoms. Greater electron charge donation to oxygen means more facile hole doping of the HfS_3 as a consequence of oxygen chemisorption. Further weak chemisorption would occur on top of the surface at the S_2^{2-} sulfur sites, and this appears to be reversible as the bulk of HfS_3 is n-type in vacuum and p-type in ambient atmosphere (as revealed by the electrical transport studies [73]).

The complex interfacial interactions of the TMTs with Au

When a metal is interfaced with a semiconductor, depending on the difference between their respective work functions, there is a possibility for the formation of a potential barrier at the metal–semiconductor interface [101]. The Schottky–Mott rule [102, 103] suggests that a Schottky barrier will form when an n-type semiconductor is brought in contact with a relatively high work function metal [101] (like Au [63–65]). Similarly, a Schottky-barrier formation can be expected at the metal/p-type semiconductor interface if a low work function metal is deposited on the surface of a p-type semiconductor with a relatively high work function. Now, one may rightly argue that the Schottky–Mott rule does not always tell the full story. This is because the chemical interactions at the metal–semiconductor interface also contribute to the resulting barrier as opposed to the difference between their work functions alone: for example, Fermi level pinning as a consequence of metal-induced gap states [104–109].

As a starting point, photoelectron spectroscopy is a good tool to ascertain the Schottky-barrier formation by measuring band bending at the semiconductor interfaces [101, 110, 111]. Such band bending manifests itself in apparent shifts in the binding energies of the photoemission core-level components, of the elements of the underlying semiconductor, as the coverage of the deposited metal increases.

Upon exposing the surface of In_4Se_3 to Au [75], a clear shift in the binding energy of the surface In $3d_{5/2}$ core-level component is observed as the Au adlayer thickness is increased (Fig. 7). To be precise, the binding energy of the surface In 3d core-level doublet is found to be lowered by ~ 0.6 eV (illustrated by solid circles in Fig. 8). However, no real dependence of the binding energy of the bulk component of the In 3d core-level doublet

© The Author(s) 2022

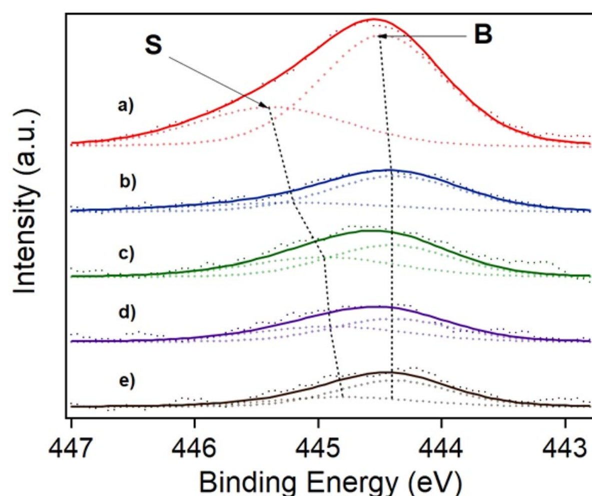

Figure 7: XPS of the In $3d_{5/2}$ core-level feature of In_4Se_3(100) crystal, with increasing Au coverage: (a) 0 nm Au, (b) 1.2 nm of Au, (c) 1.6 nm of Au, (d) 2.0 nm of Au, and (e) 2.4 nm of Au. The dashed lines denote binding energies of the surface (S) and bulk (B) In $3d_{5/2}$ core-level components [75]. © IOP Publishing. Reproduced with permission. All rights reserved.

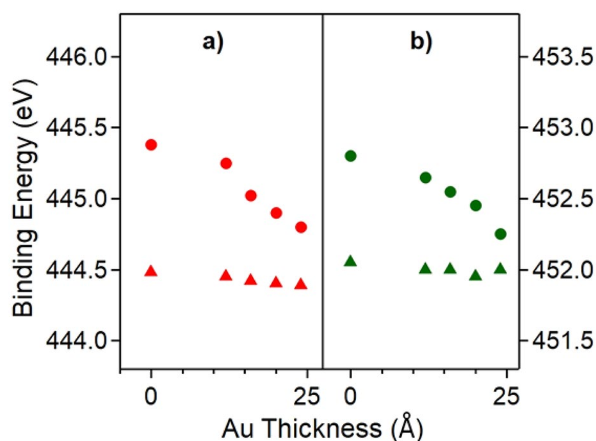

Figure 8: The changes in (a) In $3d_{5/2}$ and (b) In $3d_{3/2}$ core-level binding energies, as measured in XPS, for In_4Se_3(100) surface with increasing Au coverage. Circles depict the surface In component (indium nearest to the interface), whereas triangles represent the bulk In component (indium away from the interface) [75]. © IOP Publishing. Reproduced with permission. All rights reserved.

on the Au coverage is revealed (depicted by solid triangles in Fig. 8). Since In_4Se_3 is an n-type semiconductor [53, 75, 112] with the surface work function less than that of Au, the evident shift in the binding energy of the In 3d core-level doublet to lower values indicates upward band bending and implies the formation of an expected Schottky barrier at the Au/In_4Se_3 interface [113–118].

Since both TiS_3 and ZrS_3, like In_4Se_3, are n-type semiconducting materials [89] with relatively low work functions in comparison with that of Au [60], depositing Au on both the TMTs should also lead to the formation of a Schottky barrier at the Au/TiS_3 and Au/ZrS_3 interfaces. Contrary to the expectations based on the Schottky–Mott rule, this is not what is observed. The Au coverage-dependent XPS spectra of the S 2p and Ti 2p core-levels of TiS_3, shown in Fig. 9(a) and (b), respectively, do not show any evidence of band bending at the Au/TiS_3 interface, which implies that the Au/TiS_3 interface is actually Ohmic [74]. Likewise, deposition of Pt contacts on TiS_3 also results in an Ohmic Pt/TiS_3 interface [74], despite an extremely high work function of Pt [119]. This is likely due to an interfacial metal-sulfide formation, i.e., Au–S (or Pt–S) [72], at the Au/TiS_3 (or Pt/TiS_3) interface.

The interaction between Au and ZrS_3 does not, however, lead to an obvious Ohmic Au/ZrS_3 interface as the Au/ZrS_3 interface is somewhat more complicated [90] than the Au/TiS_3 interface. The shifts in the binding energies of the S 2p and Zr 3d core-levels of ZrS_3 as a function of Au coverage are shown in Fig. 10(a) and (10), respectively. The vertical dashed lines in Fig. 10 denote the peak XPS binding energies of S 2p and Zr 3d core-levels, whereas the horizontal dashed lines denote the shifts in binding energies. In this figure, the XPS spectra collected for the bare ZrS_3 (i.e., the XPS spectra corresponding to 0 Å of Au adlayer thickness) are at the top (in red), the XPS spectra corresponding to 4 Å of Au adlayer thickness are shown in blue, the XPS spectra corresponding to 8 Å of Au adlayer thickness are shown in green, the XPS spectra shown in purple correspond to 12 Å of Au adlayer thickness, and the spectra shown in black correspond to 16 Å of Au, respectively [90]. As the Au coverage is increased from 0 Å (spectra shown in red in Fig. 10) to 4 Å (spectra shown in blue in Fig. 10), an upward band bending, implied by the shifts in the binding energies of both the core-levels, is observed. But this band bending is found to be suppressed as a consequence of strong Au–S and Au–Zr interactions, which only get stronger as the thickness of the Au adlayer is increased further. Although the implications of such a complicated Au/ZrS_3 on the performance characteristics of ZrS_3-based nanodevices are discussed in the following section, a detailed explanation for the same is provided in ref. [90].

As discussed above, HfS_3, in spite of being isostructural with TiS_3 and ZrS_3, is more controversial in that HfS_3 has been reported to show both p-type [96] and n-type [97] semiconducting characteristics. This peculiarity of HfS_3 was addressed in an elaborate detail through a combination of XPS and electrical transport measurements [73]. Now, since chemisorption of adsorbates, like O_2, at the surface of HfS_3 renders its surface p-type and its work function is more than that of Au [60], formation of a p-type Schottky barrier may be expected at the Au/HfS_3 interface. In Fig. 11, the XPS spectra shown in red were collected for bare HfS_3 (i.e., for 0 Å of Au adlayer thickness), the XPS spectra corresponding to 6 Å of Au adlayer thickness are shown in blue, the ones shown in green correspond to 12 Å of Au adlayer thickness, and the XPS spectra shown in purple

© The Author(s) 2022

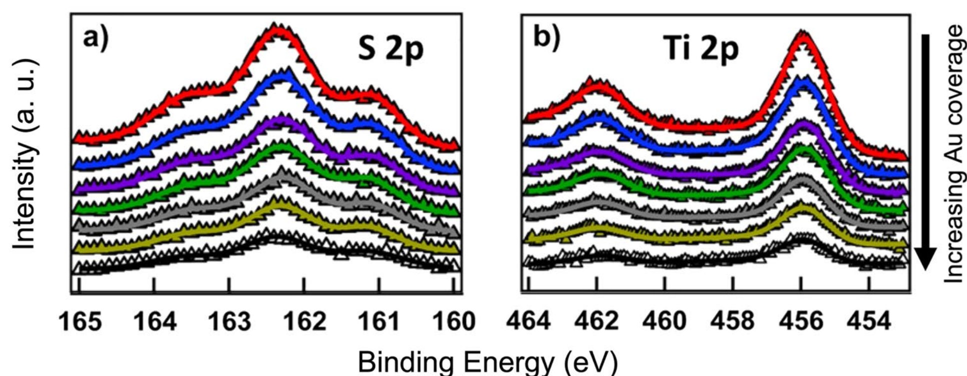

Figure 9: The XPS spectra of the (a) S 2p and (b) Ti 2p core-levels of TiS_3 as a function of Au coverage [74]. Copyright (2019) by the American Institute of Physics. Reproduced with permission. All rights reserved.

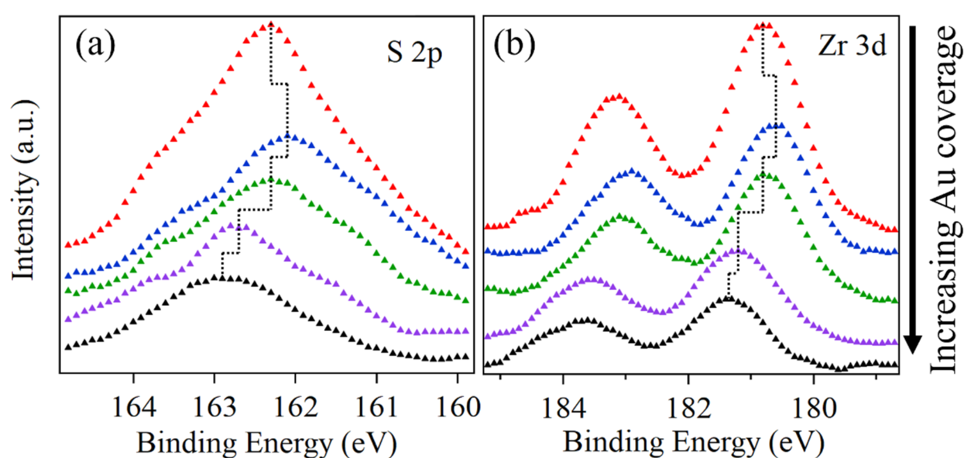

Figure 10: The XPS spectra of the (a) S 2p and (b) the Zr 3d core-level components of Au/ZrS_3(001) as a function of Au coverage [90]. © IOP Publishing. Reproduced with permission. All rights reserved.

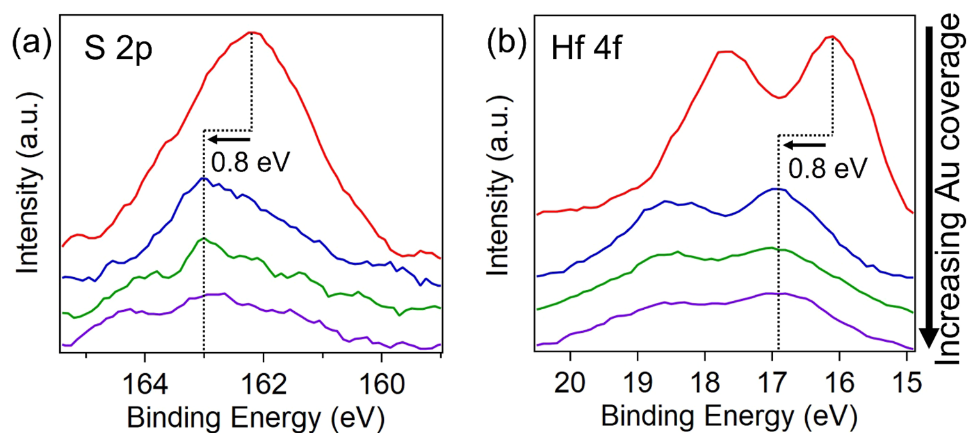

Figure 11: The photoemission spectra of (a) the S 2p and (b) Hf 4f core-levels of HfS_3 as a function of Au adlayer thickness. Reproduced from Ref. [73] with permission from the Royal Society of Chemistry.

were taken for 18 Å of Au adlayer thickness, respectively. In this figure, the peak XPS binding energies of the S 2p and Hf 4f core-levels are denoted by the vertical dashed lines, and the shift (of ~ 0.8 eV) in their respective binding energies is illustrated by the horizontal dashed line [73]. From this figure (Fig. 11), there is an unambiguous downward band bending implied by

© The Author(s) 2022

an increment in the binding energies of the S 2p and Hf 4f core-levels of HfS_3 by ~ 0.8 eV, upon interfacing with Au, confirming the formation of a p-type Schottky barrier [120–124] at the Au/HfS_3 interface.

Not only do the TMTs with different transition metal interact differently with Au, as can be inferred from the preceding discussions, but even the TMTs with the same transition metal but different chalcogens behave distinctively when interfaced with Au. One viable way to elucidate such an oddity among the TMT systems could be to compare the Au thickness-dependent XPS spectra of the core-levels of the TMTs composed of the same transition metal but different chalcogens. Therefore, capitalizing on the discussions in the preceding paragraph, let us now compare the XPS spectra shown in Fig. 11 with the Au coverage-dependent photoemission spectra of the Se 3d and Hf 4f core-levels of $HfSe_3$ (shown in Fig. 12). Upon the first deposition of Au contact (i.e., 5 Å of Au), the binding energies of both Se 3d and Hf 4f core-levels are increased by ~ 0.6 eV (spectra shown in blue in Fig. 12); thereafter, as the Au coverage is increased to 15 Å, no further change in the binding energy of the Se 3d core-level is observed. This incremental increase in the core-level binding energies of the constituent elements of $HfSe_3$ implies a p-type Schottky-barrier formation [120–124] at the Au/$HfSe_3$ interface, which is somewhat reminiscent of what was observed at the Au/HfS_3 interface. Also, here it should be noted that the shape of the spectra shown in Fig. 12(a) changes drastically as the thickness of the Au adlayer is increased. This happens because, expectedly, the XPS signal from the Au $5p_{3/2}$ core-level overpowers the XPS signal from the Se 3d core-level [125–127] as the Au coverage is increased.

Qualitatively speaking, a direct comparison of Fig. 12(a) with Fig. 11(a) indicates that the trend of the Au coverage-dependent shift in the binding energy of Se 3d core-level of $HfSe_3$ is similar to that of the S 2p core-level of HfS_3; however, this is not the case when the trends of the shifts in the binding energies of their respective Hf 4f core-levels (Figs. 12(b) and 11(b)) are compared. A closer examination reveals that the binding energy of the Hf 4f core-level of $HfSe_3$ now decreases by ~ 0.2 eV as the Au coverage increases from 5 Å (spectrum in blue in Fig. 12(b)) to 10 Å (spectrum in green in Fig. 12(b)). And this does not stop there because the binding energy of the Hf 4f core-level decreases by ~ 0.2 eV, yet again, as the Au coverage increases from 10 Å to 15 Å (spectrum in purple in Fig. 12(b)). The difference between the trends of the Au thickness-dependent binding energy shifts of the Se and Hf core-levels (Fig. 12) can be easily explained on the basis of the electronegativity argument. On the Pauling electronegativity scale, Au and Se have similar electronegativities [128–132], whereas there is a considerable difference between the electronegativities of Au and Hf [128–133]. Now since Au is more electronegative than Hf, and the downward bending of the $HfSe_3$ energy bands at the Au/$HfSe_3$ interface will lead to an accumulation of electrons at the surface of $HfSe_3$, the electrons will tend to move from Hf to Au. This motion of electrons, from Hf to Au, counteracts the downward band bending that initially happens as a result of Fermi level matching at the Au/$HfSe_3$ interface [Fig. 12(b)]; but since there is no real difference between the electronegativities of Au and Se, no such phenomenon is observed in Fig. 12(a).

Implications on characteristics of TMT-based devices

The implications of the XPS studies at the Au/TMT interfaces are reflected in the transport measurements. In consistency with the results of the photoemission measurements shown in Figs. 7 and 8, the non-Ohmic Au/In_4Se_3 interface is manifested in the *I–V* characteristics of a two-terminal In_4Se_3-based device shown

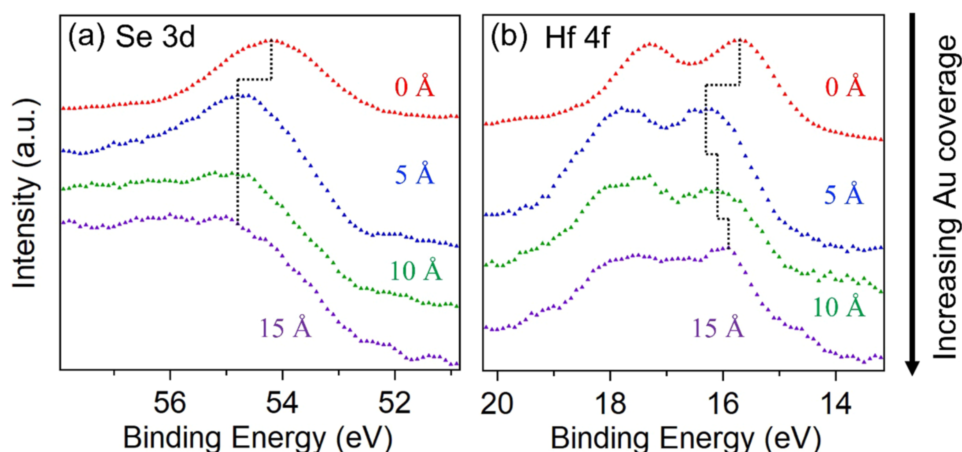

Figure 12: Variations in the (a) Se 3d core-level and (b) Hf 4f core-level photoemission spectra of $HfSe_3$ as a function of Au coverage. The binding energies of the XPS peaks of both Se 3d and Hf 4f core-levels are denoted by vertical dashed lines; and the horizontal dashed lines illustrate how the binding energy of Hf 4f core-level is decreased as the Au adlayer thickness is increased.

© The Author(s) 2022

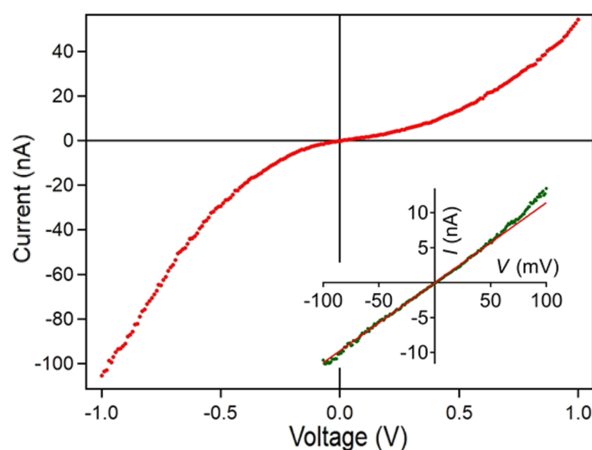

Figure 13: The *I–V* characteristics of a two-terminal In_4Se_3 devices, 20 to 40 nm thick on SiO_2, showing nonlinear behavior under no illumination (the red curve), and retention of some nonlinear behavior under 10 μW illumination at 488 nm (roughly 2.5 eV). The green curve, in the inset, is the current response under illumination, with a linear fit (red) [75]. © IOP Publishing. Reproduced with permission. All rights reserved.

in Fig. 13. Interestingly, this nonlinear *I–V* behavior is hard to avoid even when the lower work function Cr/Au contacts are used (as opposed to higher work function pure Au contacts) and the In_4Se_3 phototransistors are exposed to radiation with energy higher than its band gap (see inset of Fig. 13) [43, 75]. The Cr/Au contacts may change the electrical properties of nanoelectronic devices only slightly but the Cr–Au alloy formation leads to a sturdier physical contact in comparison with the pure Au contact [134], which is what is needed to take reliable electrical transport data for the In_4Se_3-based nanoelectronic devices.

The differences in the band bending at the Au/TiS_3, Au/ZrS_3, and Au/HfS_3 interfaces, indicated in the XPS measurements (see Figs. 9, 10, and 11) discussed above, are exhibited in the *I–V* characteristics of the FETs based on TiS_3 [Fig. 14(a)], ZrS_3 [Fig. 14(b)], and HfS_3 [Fig. 14(c)], respectively. Among these three TMTs, only the devices based on TiS_3 show linear *I–V* curves and, thus, an Ohmic behavior. The *I–V* characteristics of the ZrS_3 FET show some non-linearity at lower source-to-drain voltage (V_{DS}) and a close-to-linear behavior at higher V_{DS}. The devices with HfS_3 have a plateau of low conductance at V_{DS} between − 0.3 V and + 0.3 V, and again a close-to-linear behavior at higher V_{DS}.

These differences can be qualitatively interpreted using the model that is elaborately discussed in Ref. [135]. Based on the model given by Penumatcha et al. [135], the Au/TiS_3 interface likely has a low Schottky-barrier height. However, one cannot simply identify the range of lower conductance for ZrS_3 and HfS_3 FETs as the source-to-drain voltage overcomes the energy height of the Schottky barrier even though the height of the Schottky barrier, in each case, remains unchanged. The mechanism instead is that increasing the V_{DS} leads to the increase of the free carrier density; this decreases the geometrical width of the Schottky barrier, and the tunneling current through the barrier becomes dominant. In this case, the behavior of the contact becomes close to Ohmic, i.e., a linear dependence on V_{DS}. The influence of the gate voltage (V_G) in the case of the HfS_3 FET is such that at positive V_G it moves the Fermi level closer to the band edge and ensures higher carrier concentration and higher conductance; and at negative V_G, it moves the Fermi level away from the band edge and inhibits the thinning of the Schottky barrier.

While the electrical transport of a $HfSe_3$-based device [38] does not exactly mimic that of a HfS_3-based device [73, 96], the non-linearity in the *I-V* curves of an $HfSe_3$-based device, in agreement with the Au coverage-dependent XPS measurements on $HfSe_3$ (Fig. 12), still persists (Fig. 15).

Figure 15 shows the electrical transport of an $HfSe_3$-based device [38]. It is worth noting that while the *I–V* characteristics

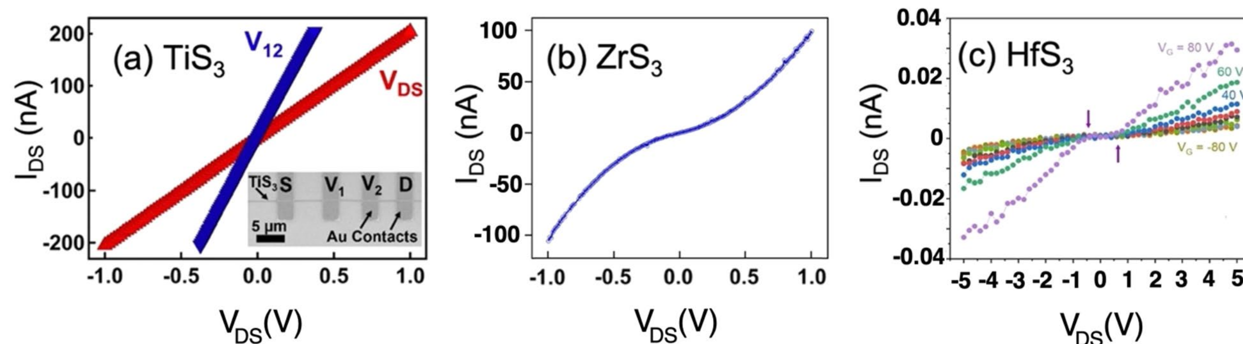

Figure 14: The electrical transport characteristics of (a) TiS_3, (b) ZrS_3, and (c) HfS_3 FETs. (a) Shows the linear *I–V* characteristics of the TiS_3 device, and (b) shows the nonlinear *I–V* characteristics of the ZrS_3 device. The I_{DS}–V_{DS} curves of the HfS_3 FET (c) were measured in vacuum, under illumination by a halogen lamp to maximize conductance, at the gate voltages (V_G) varied from -80 V to + 80 V [73]. (a) Is taken from ref. [74]. Copyright (2019) by the American Institute of Physics. Reproduced with permission. All rights reserved. (b) Is taken from Ref. [90]. © IOP Publishing. Reproduced with permission. All rights reserved. (c) Is reproduced from Ref. [73] with permission from the Royal Society of Chemistry.

© The Author(s) 2022

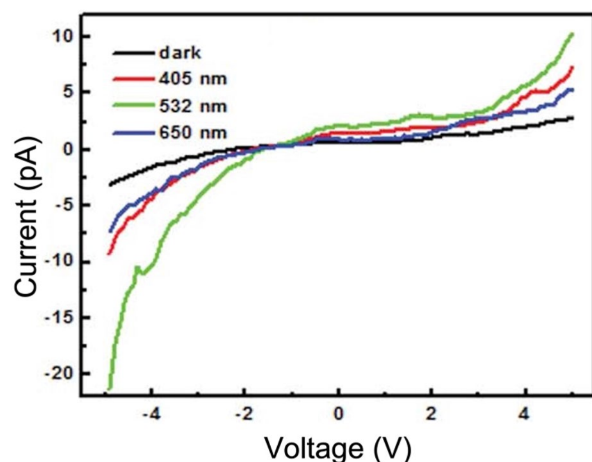

Figure 15: The nonlinear electrical transport of $HfSe_3$-based photodetector under illumination with different wavelengths of incident radiation. Reproduced from Ref. [38] with permission from the Royal Society of Chemistry.

of an $HfSe_3$-based device do not exactly mimic that of an HfS_3-based device [73, 96], the non-linearity in the *I*–*V* curves of an $HfSe_3$-based device (Fig. 15), in agreement with the Au coverage-dependent XPS measurements on $HfSe_3$ (Fig. 12), still persists.

Conclusions and future work

In conclusion, the Schottky–Mott rule alone is inadequate when explaining the Au/TMT interfaces, as the effects of the chemical interactions at these interfaces appear to play a significant role. The strength of gold–chalcogen interaction is a factor too important to disregard when explaining the nature of Au/TMT interfaces. Since the gold–chalcogen interaction can sometimes suppress the Schottky-barrier formation, this explains why the surface termination of In_4Se_3 in indium results in a Schottky barrier at the Au/In_4Se_3 interface along with the varying trends observed when Au is interfaced with TiS_3, ZrS_3, and HfS_3. In other words, the stronger the interaction between sulfur and the transition metal, the weaker the Au–S interaction. And since the electronegativity of Hf is lower than that of both Zr and Ti, the Au–S interaction at the Au/HfS_3 interface is weaker than it is at either the Au/ZrS_3 or Au/TiS_3 interface. Thus, the absence of a strong Au–S interfacial interaction (the presence of which suppresses Schottky-barrier formation at the Au/ZrS_3 [90] and Au/TiS_3 [74] interfaces) results in the formation of a Schottky barrier at the Au/HfS_3 interface. The simple electronegativity argument also sheds some light on the oddities observed in the trends of the Au thickness-dependent binding energy shifts of the Se and Hf core-levels of $HfSe_3$ (Fig. 12).

The results of photoemission spectroscopy-aided investigations [73–75, 90] of the Au/TMT interfaces are reflected in the electrical transport measurements of the devices based on these TMTs [52, 73–75, 90, 96, 136]. Among all the TMTs reviewed herein, only the devices based on TiS_3 show Ohmic behavior, while the devices derived from the rest of the TMTs do not. Nevertheless, there are a few ways that can help circumvent this issue in the foreseeable future: (i) dope the contact regions degenerately to manipulate the Schottky-barrier height [137, 138]; (ii) select the contact metals with the right work function with respect to the semiconducting type of the TMT of interest [139] (i.e., selecting high work function metals for p-type TMTs [140–144] and low work function metals for the n-type ones [53, 75, 89, 112]); (iii) use ionic-liquid gates to reduce the Schottky-barrier height [145]; and (iv) pick contact materials whose work function can be tuned as needed [146].

Acknowledgments

This work was supported by National Science Foundation through EPSCoR RII Track-1: Emergent Quantum Materials and Technologies (EQUATE), Award OIA-2044049.

Data availability

The datasets generated during and/or analyzed during the current study are available from the corresponding author on reasonable request.

Declarations

Conflict of interest On behalf of all authors, the corresponding author states that there is no conflict of interest.

Open Access

This article is licensed under a Creative Commons Attribution 4.0 International License, which permits use, sharing, adaptation, distribution and reproduction in any medium or format, as long as you give appropriate credit to the original author(s) and the source, provide a link to the Creative Commons licence, and indicate if changes were made. The images or other third party material in this article are included in the article's Creative Commons licence, unless indicated otherwise in a credit line to the material. If material is not included in the article's Creative Commons licence and your intended use is not permitted by statutory regulation or exceeds the permitted use, you will need to obtain permission directly from the copyright holder. To view a copy of this licence, visit http://creativecommons.org/licenses/by/4.0/.

© The Author(s) 2022

References

1. R.R. Troutman, VLSI limitations from drain-induced barrier lowering. IEEE J. Solid-State Circuits **14**(2), 383 (1979). https://doi.org/10.1109/JSSC.1979.1051189
2. S.G. Chamberlain, S. Ramanan, Drain-induced barrier-lowering analysis in VSLI MOSFET devices using two-dimensional numerical simulations. IEEE Trans. Electron Devices **33**(11), 1745 (1986). https://doi.org/10.1109/T-ED.1986.22737
3. A.A. Mutlu, M. Rahman: in *Proceedings of the IEEE SoutheastCon 2000. 'Preparing for The New Millennium' (Cat. No.00CH37105)* (IEEE, 2000), pp. 340–344. https://doi.org/10.1109/SECON.2000.845589.
4. J.A. Adams, I.G. Thayne, C.D.W. Wilkinson, S.P. Beaumont, N.P. Johnson, A.K. Kean, C.R. Stanley, Short-channel effects and drain-induced barrier lowering in nanometer-scale GaAs MESFET's. IEEE Trans. Electron Devices **40**(6), 1047 (1993). https://doi.org/10.1109/16.214727
5. D. Sarkar, X. Xie, W. Liu, W. Cao, J. Kang, Y. Gong, S. Kraemer, P.M. Ajayan, K. Banerjee, A subthermionic tunnel field-effect transistor with an atomically thin channel. Nature **526**(7571), 91 (2015). https://doi.org/10.1038/nature15387
6. R.-H. Yan, A. Ourmazd, K.F. Lee, Scaling the Si MOSFET: from bulk to SOI to bulk. IEEE Trans. Electron Devices **39**(7), 1704 (1992). https://doi.org/10.1109/16.141237
7. I. Ferain, C.A. Colinge, J.-P. Colinge, Multigate transistors as the future of classical metal–oxide–semiconductor field-effect transistors. Nature **479**(7373), 310 (2011). https://doi.org/10.1038/nature10676
8. J.-T. Park, J.-P. Colinge, Multiple-gate SOI MOSFETs: device design guidelines. IEEE Trans. Electron Devices **49**(12), 2222 (2002). https://doi.org/10.1109/TED.2002.805634
9. S. Furuseth, L. Brattas, A. Kjekshus, On the crystal structures of TiS_3, ZrS_3, $ZrSe_3$, $ZrTe_3$, HfS_3, and $HfSe_3$. Acta Chem. Scand. **29**(6), 623 (1975)
10. S.K. Srivastava, B.N. Avasthi, Preparation, structure and properties of transition metal trichalcogenides. J. Mater. Sci. **27**(14), 3693 (1992). https://doi.org/10.1007/BF00545445
11. J. Dai, M. Li, X.C. Zeng, Group IVB transition metal trichalcogenides: a new class of 2D layered materials beyond graphene. Wiley Interdiscip. Rev. Comput. Mol. Sci. **6**(2), 211 (2016). https://doi.org/10.1002/wcms.1243
12. J.O. Island, M. Barawi, R. Biele, A. Almazán, J.M. Clamagirand, J.R. Ares, C. Sánchez, H.S.J. van der Zant, J.V. Álvarez, R. D'Agosta, I.J. Ferrer, A. Castellanos-Gomez, TiS_3 transistors with tailored morphology and electrical properties. Adv. Mater. **27**(16), 2595 (2015). https://doi.org/10.1002/adma.201405632
13. A. Lipatov, M.J. Loes, H. Lu, J. Dai, P. Patoka, N.S. Vorobeva, D.S. Muratov, G. Ulrich, B. Kästner, A. Hoehl, G. Ulm, X.C. Zeng, E. Rühl, A. Gruverman, P.A. Dowben, A. Sinitskii, Quasi-1D TiS_3 nanoribbons: mechanical exfoliation and thickness-dependent raman spectroscopy. ACS Nano **12**(12), 12713 (2018). https://doi.org/10.1021/acsnano.8b07703
14. J. Dai, X.C. Zeng, Titanium trisulfide monolayer: theoretical prediction of a new direct-gap semiconductor with high and anisotropic carrier mobility. Angew. Chem. Int. Ed. **54**(26), 7572 (2015). https://doi.org/10.1002/anie.201502107
15. D.W. Bullett, Variation of electronic properties with structure of transition metal trichalcogenides. J. Phys. C Solid State Phys. **12**(2), 277 (1979). https://doi.org/10.1088/0022-3719/12/2/015
16. M.D. Randle, A. Lipatov, I. Mansaray, J.E. Han, A. Sinitskii, J.P. Bird, Collective states and charge density waves in the group IV transition metal trichalcogenides. Appl. Phys. Lett. **118**(21), 210502 (2021). https://doi.org/10.1063/5.0052295
17. A. Zwick, M.A. Renucci, A. Kjekshus, Raman scattering in the IVB transition-metal trichalcogenides: ZrS_3, $ZrSe_3$, $ZrTe_3$ and $HfSe_3$. J. Phys. C Solid State Phys. **13**(30), 5603 (1980). https://doi.org/10.1088/0022-3719/13/30/023
18. E.R. Mucciolo, C.H. Lewenkopf, Disorder and electronic transport in graphene. J. Phys. Condens. Matter **22**(27), 273201 (2010). https://doi.org/10.1088/0953-8984/22/27/273201
19. F. Banhart, J. Kotakoski, A.V. Krasheninnikov, Structural defects in graphene. ACS Nano **5**(1), 26 (2010). https://doi.org/10.1021/NN102598M
20. R. Debbarma, N.H.L. Nguyen, V. Berry, Defect guided conduction in graphene-derivatives and MoS_2: two-dimensional nanomaterial models. Appl. Mater. Today **23**, 101072 (2021). https://doi.org/10.1016/J.APMT.2021.101072
21. H.-P. Komsa, J. Kotakoski, S. Kurasch, O. Lehtinen, U. Kaiser, A.V. Krasheninnikov, Two-dimensional transition metal dichalcogenides under electron irradiation: defect production and doping. Phys. Rev. Lett. **109**(3), 035503 (2012). https://doi.org/10.1103/PhysRevLett.109.035503
22. S.-T. Lo, O. Klochan, C.-H. Liu, W.-H. Wang, A.R. Hamilton, C.-T. Liang, Transport in disordered monolayer MoS_2 nanoflakes—evidence for inhomogeneous charge transport. Nanotechnology **25**(37), 375201 (2014). https://doi.org/10.1088/0957-4484/25/37/375201
23. R. Addou, L. Colombo, R.M. Wallace, Surface defects on natural MoS_2. ACS Appl. Mater. Interfaces **7**(22), 11921 (2015). https://doi.org/10.1021/acsami.5b01778
24. Z. Lin, B.R. Carvalho, E. Kahn, R. Lv, R. Rao, H. Terrones, M.A. Pimenta, M. Terrones, Defect engineering of two-dimensional transition metal dichalcogenides. 2D Mater. **3**(2), 022002 (2016). https://doi.org/10.1088/2053-1583/3/2/022002
25. M.R. Rosenberger, H.-J. Chuang, K.M. McCreary, C.H. Li, B.T. Jonker, Electrical characterization of discrete defects and impact of defect density on photoluminescence in monolayer WS_2. ACS Nano **12**(2), 1793 (2018). https://doi.org/10.1021/ACSNANO.7B08566

© The Author(s) 2022

26. W.H. Blades, N.J. Frady, P.M. Litwin, S.J. McDonnell, P. Reinke, Thermally induced defects on WSe_2. J. Phys. Chem. C **124**(28), 15337 (2020). https://doi.org/10.1021/ACS.JPCC.0C04440
27. M. Wimmer, İ Adagideli, S. Berber, D. Tománek, K. Richter, Spin currents in rough graphene nanoribbons: universal fluctuations and spin injection. Phys. Rev. Lett. **100**(17), 177207 (2008). https://doi.org/10.1103/PhysRevLett.100.177207
28. J. Wurm, K. Richter, İ Adagideli, Edge effects in graphene nanostructures: from multiple reflection expansion to density of states. Phys. Rev. B **84**(7), 075468 (2011). https://doi.org/10.1103/PhysRevB.84.075468
29. V.K. Dugaev, M.I. Katsnelson, Edge scattering of electrons in graphene: Boltzmann equation approach to the transport in graphene nanoribbons and nanodisks. Phys. Rev. B **88**(23), 235432 (2013). https://doi.org/10.1103/PhysRevB.88.235432
30. Y.-J. Shi, J. Lan, E.-J. Ye, W.-Q. Sui, X. Zhao, Four-terminal impedance of a graphene nanoribbon based structure. Eur. Phys. J. B **87**(10), 251 (2014). https://doi.org/10.1140/epjb/e2014-50321-0
31. L. Dong, J. Wang, R. Namburu, T.P. O'Regan, M. Dubey, A.M. Dongare, Edge effects on band gap energy in bilayer 2H-MoS_2 under uniaxial strain. J. Appl. Phys. **117**(24), 244303 (2015). https://doi.org/10.1063/1.4922811
32. V. Mlinar, Electronic and optical properties of nanostructured MoS_2 materials: influence of reduced spatial dimensions and edge effects. Phys. Chem. Chem. Phys. **19**(24), 15891 (2017). https://doi.org/10.1039/C7CP03229C
33. F. Saiz, J. Carrete, R. Rurali, Anisotropic thermal conductivity in few-layer and bulk titanium trisulphide from first principles. Nanomaterials **10**(4), 704 (2020). https://doi.org/10.3390/nano10040704
34. Y. Jin, X. Li, J. Yang, Single layer of MX_3 (M = Ti, Zr; X = S, Se, Te): a new platform for nano-electronics and optics. Phys. Chem. Chem. Phys. **17**(28), 18665 (2015). https://doi.org/10.1039/c5cp02813b
35. R. Biele, R. D'Agosta, Transport coefficients of layered TiS_3. Phys. Rev. Mater. **6**(1), 014004 (2022). https://doi.org/10.1103/PhysRevMaterials.6.014004
36. W. Zhang, T. Lv, C. Deng, H. Gao, S. Hu, F. Chen, J. Liu, X. Fan, Y. Liu, B. Jiao, L. Deng, W. Xiong, Rapid solid-phase sulfurization growth and nonlinear optical characterization of transfer-free TiS_3 nanoribbons. Chem. Mater. **34**(6), 2790 (2022). https://doi.org/10.1021/acs.chemmater.2c00068
37. M.D. Randle, A. Lipatov, A. Datta, A. Kumar, I. Mansaray, A. Sinitskii, U. Singisetti, J.E. Han, J.P. Bird, High-electric-field behavior of the metal-insulator transition in TiS_3 nanowire transistors. Appl. Phys. Lett. **120**(7), 073102 (2022). https://doi.org/10.1063/5.0083166
38. W.-W. Xiong, J.-Q. Chen, X.-C. Wu, J.-J. Zhu, Visible light detectors based on individual $ZrSe_3$ and $HfSe_3$ nanobelts. J. Mater. Chem. C **3**(9), 1929 (2015). https://doi.org/10.1039/C4TC02492C
39. J.O. Island, A.J. Molina-Mendoza, M. Barawi, R. Biele, E. Flores, J.M. Clamagirand, J.R. Ares, C. Sánchez, H.S.J. van der Zant, R. D'Agosta, I.J. Ferrer, A. Castellanos-Gomez, Electronics and optoelectronics of quasi-1D layered transition metal trichalcogenides. 2D Mater. **4**(2), 022003 (2017). https://doi.org/10.1088/2053-1583/aa6ca6
40. A. Patra, C.S. Rout, Anisotropic quasi-one-dimensional layered transition-metal trichalcogenides: synthesis, properties and applications. RSC Adv. **10**(60), 36413 (2020). https://doi.org/10.1039/D0RA07160A
41. X. Yu, X. Wen, W. Zhang, L. Yang, H. Wu, X. Lou, Z. Xie, Y. Liu, H. Chang, Fast and controlled growth of two-dimensional layered $ZrTe_3$ nanoribbons by chemical vapor deposition. CrystEngComm **21**(37), 5586 (2019). https://doi.org/10.1039/C9CE00793H
42 S. Hou, Z. Guo, J. Yang, Y. Liu, W. Shen, C. Hu, S. Liu, H. Gu, Z. Wei, Birefringence and dichroism in Quasi-1D transition metal trichalcogenides: direct experimental investigation. Small (2021). https://doi.org/10.1002/smll.202100457
43. A. Dhingra, S.J. Gilbert, J.-S. Chen, P.V. Galiy, T.M. Nenchuk, P.A. Dowben, Power and polarization-dependent photoresponse of quasi-one-dimensional In_4Se_3. MRS Adv. (2022). https://doi.org/10.1557/s43580-022-00259-6
44. Y.R. Tao, J.J. Wu, X.C. Wu, Enhanced ultraviolet-visible light responses of phototransistors based on single and a few ZrS_3 nanobelts. Nanoscale **7**(34), 14292 (2015). https://doi.org/10.1039/c5nr03589a
45. A. Patel, K.D.K. Patel, C. Limberkar, V. Jethwa, K.D.K. Patel, G.K. Solanki, V.M. Pathak, Tunable anisotropic pulse photo response of ZrS_3 crystal at cryogenic temperatures. Phys. B Condens. Matter **633**, 413775 (2022). https://doi.org/10.1016/j.physb.2022.413775
46. A. Patra, S. Kapse, R. Thapa, D.J. Late, C.S. Rout, Quasi-one-dimensional van der Waals TiS_3 nanosheets for energy storage applications: theoretical predications and experimental validation. Appl. Phys. Lett. **120**(10), 103102 (2022). https://doi.org/10.1063/5.0080346
47. H. Kamimura (ed.), *Theoretical Aspects of Band Structures and Electronic Properties of Pseudo-One-Dimensional Solids* (Springer, Dordrecht, 1985). https://doi.org/10.1007/978-94-009-5299-7
48. Y.B. Losovyj, L. Makinistian, E.A. Albanesi, A.G. Petukhov, J. Liu, P. Galiy, O.R. Dveriy, P.A. Dowben, The anisotropic band structure of layered In_4Se_3(001). J. Appl. Phys. **104**(8), 083713 (2008). https://doi.org/10.1063/1.3000453
49. W. Kong, C. Bacaksiz, B. Chen, K. Wu, M. Blei, X. Fan, Y. Shen, H. Sahin, D. Wright, D.S. Narang, S. Tongay, Angle resolved vibrational properties of anisotropic transition metal

© The Author(s) 2022

trichalcogenide nanosheets. Nanoscale **9**(12), 4175 (2017). https://doi.org/10.1039/c7nr00711f

50. Y.B. Losovyj, M. Klinke, E. Cai, I. Rodriguez, J. Zhang, L. Makinistian, A.G. Petukhov, E.A. Albanesi, P. Galiy, Y. Fiyala, J. Liu, P.A. Dowben, The electronic structure of surface chains in the layered semiconductor In_4Se_3(100). Appl. Phys. Lett. **92**(12), 122107 (2008). https://doi.org/10.1063/1.2894577
51 A. Khatibi, R.H. Godiksen, S.B. Basuvalingam, D. Pellegrino, A.A. Bol, B. Shokri, A.G. Curto, Anisotropic infrared light emission from quasi-1D layered TiS_3. 2D Mater. **7**(1), 015022 (2020). https://doi.org/10.1088/2053-1583/ab57ef
52. S.J. Gilbert, H. Yi, J.-S. Chen, A.J. Yost, A. Dhingra, J. Abourahma, A. Lipatov, J. Avila, T. Komesu, A. Sinitskii, M.C. Asensio, P.A. Dowben, Effect of band symmetry on photocurrent production in quasi-one-dimensional transition-metal trichalcogenides. ACS Appl. Mater. Interfaces **12**(36), 40525 (2020). https://doi.org/10.1021/acsami.0c11892
53. N.S. Vorobeva, A. Lipatov, A. Torres, J. Dai, J. Abourahma, D. Le, A. Dhingra, S.J. Gilbert, P.V. Galiy, T.M. Nenchuk, D.S. Muratov, T.S. Rahman, X.C. Zeng, P.A. Dowben, A. Sinitskii, Anisotropic properties of quasi-1D In_4Se_3: mechanical exfoliation, electronic transport, and polarization-dependent photoresponse. Adv. Funct. Mater. (2021). https://doi.org/10.1002/ADFM.202106459
54. S. Liu, W. Xiao, M. Zhong, L. Pan, X. Wang, H.-X. Deng, J. Liu, J. Li, Z. Wei, Highly polarization sensitive photodetectors based on quasi-1D titanium trisulfide (TiS_3). Nanotechnology **29**(18), 184002 (2018). https://doi.org/10.1088/1361-6528/aaafa2
55. X. Wang, K. Wu, M. Blei, Y. Wang, L. Pan, K. Zhao, C. Shan, M. Lei, Y. Cui, B. Chen, D. Wright, W. Hu, S. Tongay, Z. Wei, Highly Polarized photoelectrical response in vdW ZrS_3 nanoribbons. Adv. Electron. Mater. **5**(7), 1900419 (2019). https://doi.org/10.1002/aelm.201900419
56. J.O. Island, R. Biele, M. Barawi, J.M. Clamagirand, J.R. Ares, C. Sánchez, H.S.J. van der Zant, I.J. Ferrer, R. D'Agosta, A. Castellanos-Gomez, Titanium trisulfide (TiS_3): a 2D semiconductor with quasi-1D optical and electronic properties. Sci. Rep. **6**(1), 22214 (2016). https://doi.org/10.1038/srep22214
57 D.S. Schulman, A.J. Arnold, S. Das, Contact engineering for 2D materials and devices. Chem. Soc. Rev. **47**(9), 3037 (2018). https://doi.org/10.1039/C7CS00828G
58 L.-W. Wong, L. Huang, F. Zheng, Q.H. Thi, J. Zhao, Q. Deng, T.H. Ly, Site-specific electrical contacts with the two-dimensional materials. Nat. Commun. **11**(1), 1 (2020). https://doi.org/10.1038/s41467-020-17784-3
59. S. Chen, S. Wang, C. Wang, Z. Wang, Q. Liu, Latest advance on seamless metal-semiconductor contact with ultralow Schottky barrier in 2D-material-based devices. Nano Today **42**, 101372 (2022). https://doi.org/10.1016/j.nantod.2021.101372
60. Q. Zhao, Y. Guo, Y. Zhou, Z. Yao, Z. Ren, J. Bai, X. Xu, Band alignments and heterostructures of monolayer transition metal trichalcogenides MX_3 (M = Zr, Hf; X = S, Se) and dichalcogenides MX_2 (M = Tc, Re; X=S, Se) for solar applications. Nanoscale **10**(7), 3547 (2018). https://doi.org/10.1039/C7NR08413G
61. E.H. Rhoderick, R.H. Williams, *Metal-semiconductor contacts*, 2nd edn. (Oxford University Press, New York, 1988)
62. M. Kaltenbrunner, G. Adam, E.D. Głowacki, M. Drack, R. Schwödiauer, L. Leonat, D.H. Apaydin, H. Groiss, M.C. Scharber, M.S. White, N.S. Sariciftci, S. Bauer, Flexible high power-per-weight perovskite solar cells with chromium oxide–metal contacts for improved stability in air. Nat. Mater. **14**(10), 1032 (2015). https://doi.org/10.1038/nmat4388
63. D.E. Eastman, Photoelectric work functions of transition, rare-earth, and noble metals. Phys. Rev. B **2**(1), 1 (1970). https://doi.org/10.1103/PhysRevB.2.1
64. H.C. Potter, J.M. Blakely, LEED, Auger spectroscopy, and contact potential studies of copper–gold alloy single crystal surfaces. J. Vac. Sci. Technol. **12**(2), 635 (1975). https://doi.org/10.1116/1.568637
65. H. Kawano, Effective work functions for ionic and electronic emissions from mono- and polycrystalline surfaces. Prog. Surf. Sci. **83**(1–2), 1 (2008). https://doi.org/10.1016/j.progsurf.2007.11.001
66. K. Fukutani, T. Sato, P.V. Galiy, K. Sugawara, T. Takahashi, Tunable two-dimensional electron gas at the surface of thermoelectric material In_4Se_3. Phys. Rev. B **93**(20), 205156 (2016). https://doi.org/10.1103/PhysRevB.93.205156
67. Q. Cui, A. Lipatov, J.S. Wilt, M.Z. Bellus, X.C. Zeng, J. Wu, A. Sinitskii, H. Zhao, Time-resolved measurements of photocarrier dynamics in TiS_3 nanoribbons. ACS Appl. Mater. Interfaces **8**(28), 18334 (2016). https://doi.org/10.1021/acsami.6b04092
68. H. Yi, T. Komesu, S. Gilbert, G. Hao, A.J. Yost, A. Lipatov, A. Sinitskii, J. Avila, C. Chen, M.C. Asensio, P.A. Dowben, The band structure of the quasi-one-dimensional layered semiconductor TiS_3(001). Appl. Phys. Lett. **112**(5), 052102 (2018). https://doi.org/10.1063/1.5020054
69. A. Dhingra, A. Lipatov, M.J. Loes, A. Sinitskii, P.A. Dowben, Nonuniform Debye temperatures in quasi-one-dimensional transition-metal trichalcogenides. ACS Mater. Lett. **3**(4), 414 (2021). https://doi.org/10.1021/acsmaterialslett.1c00094
70. D.S. Muratov, A.R. Ishteev, D.A. Lypenko, V.O. Vanyushin, P. Gostishev, S. Perova, D.S. Saranin, D. Rossi, M. Auf der Maur, G. Volonakis, F. Giustino, P.O.Å. Persson, D.V. Kuznetsov, A. Sinitskii, A. Di Carlo, Slot-die-printed two-dimensional ZrS_3 charge transport layer for perovskite light-emitting diodes. ACS Appl. Mater. Interfaces **11**(51), 48021 (2019). https://doi.org/10.1021/acsami.9b16457
71. D.S. Muratov, V.O. Vanyushin, N.S. Vorobeva, P. Jukova, A. Lipatov, E.A. Kolesnikov, D. Karpenkov, D.V. Kuznetsov, A. Sinitskii, Synthesis and exfoliation of quasi-1D (Zr, Ti)$_S$3 solid solutions for device measurements. J. Alloys Compd. **815**, 152316 (2020). https://doi.org/10.1016/j.jallcom.2019.152316

© The Author(s) 2022

72. H. Haraldsen, A. Kjekshus, E. Røst, A. Steffensen, J. Munch-Petersen, On the properties of TiS_3, ZrS_3, and HfS_3. Acta Chem. Scand. **17**, 1283 (1963). https://doi.org/10.3891/acta.chem.scand.17-1283
73. A. Dhingra, A. Lipatov, M.J. Loes, J. Abourahma, M. Pink, A. Sinitskii, P.A. Dowben, Effect of Au/HfS_3 interfacial interactions on properties of HfS_3-based devices. Phys. Chem. Chem. Phys. **24**(22), 14016 (2022). https://doi.org/10.1039/D2CP01254E
74. S.J. Gilbert, A. Lipatov, A.J. Yost, M.J. Loes, A. Sinitskii, P.A. Dowben, The electronic properties of Au and Pt metal contacts on quasi-one-dimensional layered TiS_3(001). Appl. Phys. Lett. **114**(10), 101604 (2019). https://doi.org/10.1063/1.5090270
75. A. Dhingra, P.V. Galiy, L. Wang, N.S. Vorobeva, A. Lipatov, A. Torres, T.M. Nenchuk, S.J. Gilbert, A. Sinitskii, A.J. Yost, W.-N. Mei, K. Fukutani, J.-S. Chen, P.A. Dowben, Surface termination and Schottky-barrier formation of In_4Se_3(001). Semicond. Sci. Technol. **35**(6), 065009 (2020). https://doi.org/10.1088/1361-6641/ab7e45
76. A. Dhingra, D. Sando, P.-S. Lu, Z.G. Marzouk, V. Nagarajan, P.A. Dowben, X-ray photoemission studies of $BiInO_3$: surface termination and effective Debye temperature. J. Appl. Phys. **130**(2), 025304 (2021). https://doi.org/10.1063/5.0057556
77. Y. Bai, X. Meng, S. Yang, Interface engineering for highly efficient and stable planar p-i-n perovskite solar cells. Adv. Energy Mater. **8**(5), 1701883 (2018). https://doi.org/10.1002/aenm.201701883
78. H. Zhang, Y. Li, X. Zhang, Y. Zhang, H. Zhou, Role of interface properties in organic solar cells: from substrate engineering to bulk-heterojunction interfacial morphology. Mater. Chem. Front. **4**(10), 2863 (2020). https://doi.org/10.1039/D0QM00398K
79. R.W. Paynter, An ARXPS primer. J. Electron Spectrosc. Relat. Phenomena **169**(1), 1 (2009). https://doi.org/10.1016/j.elspec.2008.09.005
80. S.D. Gardner, C.S.K. Singamsetty, G.L. Booth, G.-R. He, C.U. Pittman, Surface characterization of carbon fibers using angle-resolved XPS and ISS. Carbon N. Y. **33**(5), 587 (1995). https://doi.org/10.1016/0008-6223(94)00144-O
81. J.B. Gilbert, M.F. Rubner, R.E. Cohen, Depth-profiling X-ray photoelectron spectroscopy (XPS) analysis of interlayer diffusion in polyelectrolyte multilayers. Proc. Natl. Acad. Sci. USA **110**(17), 6651 (2013). https://doi.org/10.1073/pnas.1222325110
82. K.L. Parry, A.G. Shard, R.D. Short, R.G. White, J.D. Whittle, A. Wright, ARXPS characterisation of plasma polymerised surface chemical gradients. Surf. Interfaces Anal. **38**(11), 1497 (2006). https://doi.org/10.1002/sia.2400
83. M.P. Seah, W.A. Dench, Quantitative electron spectroscopy of surfaces: a standard data base for electron inelastic mean free paths in solids. Surf. Interfaces Anal. **1**(1), 2 (1979). https://doi.org/10.1002/sia.740010103
84. J.C. Ashley, C.J. Tung, Electron inelastic mean free paths in several solids for 200 eV $\leq E \leq$ 10 keV. Surf. Interfaces Anal. **4**(2), 52 (1982). https://doi.org/10.1002/sia.740040205
85. W.A.M. Aarnink, A. Weishaupt, A. van Silfhout, Angle-resolved X-ray photoelectron spectroscopy (ARXPS) and a modified Levenberg-Marquardt fit procedure: a new combination for modeling thin layers. Appl. Surf. Sci. **45**(1), 37 (1990). https://doi.org/10.1016/0169-4332(90)90018-U
86 J.H.C. Hogg, H.H. Sutherland, D.J. Williams, The crystal structure of tetraindium triselenide. Acta Crystallogr. Sect. B Struct. Crystallogr. Cryst. Chem. **29**(8), 1590 (1973). https://doi.org/10.1107/S0567740873005108
87 J. Liu, Y.B. Losovyj, T. Komesu, P.A. Dowben, L. Makinistian, E.A. Albanesi, A.G. Petukhov, P. Galiy, Y. Fiyala, The bulk band structure and inner potential of layered In_4Se_3. Appl. Surf. Sci. (2008). https://doi.org/10.1016/j.apsusc.2008.01.061
88. A. Dhingra, Z.G. Marzouk, E. Mishra, P.V. Galiy, T.M. Nenchuk, P.A. Dowben, Indium segregation to the selvedge of In_4Se_3(001). Phys. B Condens. Matter **593**, 412280 (2020). https://doi.org/10.1016/j.physb.2020.412280
89 H. Yi, S.J. Gilbert, A. Lipatov, A. Sinitskii, J. Avila, J. Abourahma, T. Komesu, M.C. Asensio, P.A. Dowben, The electronic band structure of quasi-one-dimensional van der Waals semiconductors: the effective hole mass of ZrS_3 compared to TiS_3. J. Phys. Condens. Matter **32**(29), 29LT01 (2020). https://doi.org/10.1088/1361-648X/ab832c
90. A. Dhingra, A. Lipatov, A. Sinitskii, P.A. Dowben, Complexities at the Au/ZrS_3(001) interface probed by X-ray photoemission spectroscopy. J. Phys. Condens. Matter **33**(43), 434001 (2021). https://doi.org/10.1088/1361-648X/ac16f8
91. D.D. Sarma, C.N.R. Rao, XPES studies of oxides of second- and third-row transition metals including rare earths. J. Electron Spectros. Relat. Phenomena **20**(1), 25 (1980). https://doi.org/10.1016/0368-2048(80)85003-1
92. G.D. Wilk, R.M. Wallace, J.M. Anthony, Hafnium and zirconium silicates for advanced gate dielectrics. J. Appl. Phys. **87**(1), 484 (1999). https://doi.org/10.1063/1.371888
93. H.Y. Yu, M.F. Li, B.J. Cho, C.C. Yeo, M.S. Joo, D.-L. Kwong, J.S. Pan, C.H. Ang, J.Z. Zheng, S. Ramanathan, Energy gap and band alignment for $(HfO_2)_x(Al_2O_3)_{1-x}$ on (100) Si. Appl. Phys. Lett. **81**(2), 376 (2002). https://doi.org/10.1063/1.1492024
94. N. Zhan, M.C. Poon, C.W. Kok, K.L. Ng, H. Wong, XPS study of the thermal instability of HfO_2 prepared by Hf sputtering in oxygen with RTA. J. Electrochem. Soc. **150**(10), F200 (2003). https://doi.org/10.1149/1.1608006
95. D. Barreca, A. Milanov, R.A. Fischer, A. Devi, E. Tondello, Hafnium oxide thin film grown by ALD: an XPS study. Surf. Sci. Spectra **14**, 34 (2007). https://doi.org/10.1116/11.20080401
96. W.W. Xiong, J.Q. Chen, X.C. Wu, J.J. Zhu, Individual HfS_3 nanobelt for field-effect transistor and high performance visible-light detector. J. Mater. Chem. C **2**(35), 7392 (2014). https://doi.org/10.1039/c4tc01039f

© The Author(s) 2022

97 E. Flores, J.R. Ares, I.J. Ferrer, C. Sánchez, Synthesis and characterization of a family of layered trichalcogenides for assisted hydrogen photogeneration. Phys. Status Solidi Rapid Res. Lett. **10**(11), 802 (2016). https://doi.org/10.1002/pssr.201600169
98. A. Dhingra, Comment on "Rapid solid-phase sulfurization growth and nonlinear optical characterization of transfer-free TiS_3 nanoribbons." Chem. Mater. **34**(15), 7090 (2022). https://doi.org/10.1021/acs.chemmater.2c01122
99. W. Zhang, T. Lv, C. Deng, L. Zhou, C. Wei, H. Gao, S. Hu, F. Chen, J. Liu, X. Fan, Y. Liu, B. Jiao, L. Deng, W. Xiong, Reply to Comment on "Rapid solid-phase sulfurization growth and nonlinear optical characterization of transfer-free TiS_3 nanoribbons." Chem. Mater. **34**(15), 7091–7092 (2022). https://doi.org/10.1021/acs.chemmater.2c01693
100. F. Iyikanat, H. Sahin, R.T. Senger, F.M. Peeters, Vacancy formation and oxidation characteristics of single layer TiS_3. J. Phys. Chem. C **119**(19), 10709 (2015). https://doi.org/10.1021/acs.jpcc.5b01562
101. Z. Zhang, J.T. Yates, Band bending in semiconductors: chemical and physical consequences at surfaces and interfaces. Chem. Rev. **112**(10), 5520 (2012). https://doi.org/10.1021/cr3000626
102. W. Schottky, Zur Halbleitertheorie der Sperrschicht- und Spitzengleichrichter. Z. für Phys. **113**(5–6), 367 (1939). https://doi.org/10.1007/BF01340116
103. N.F. Mott, The theory of crystal rectifiers. Proc. R. Soc. A **171**(944), 153 (1939). https://doi.org/10.1142/9789812794086_0013
104. J. Bardeen, Surface states and rectification at a metal semi-conductor contact. Phys. Rev. **71**(10), 717 (1947). https://doi.org/10.1103/PhysRev.71.717
105. W. Mönch, Valence-band offsets and Schottky barrier heights of layered semiconductors explained by interface-induced gap states. Appl. Phys. Lett. **72**(15), 1899 (1998). https://doi.org/10.1063/1.121220
106 W. Mönch, Barrier heights of real Schottky contacts explained by metal-induced gap states and lateral inhomogeneities. J. Vac. Sci. Technol. B Microelectron. Nanom. Struct. **17**(4), 1867 (1999). https://doi.org/10.1116/1.590839
107. R.T. Tung, Chemical bonding and fermi level pinning at metal-semiconductor interfaces. Phys. Rev. Lett. **84**(26), 6078 (2000). https://doi.org/10.1103/PhysRevLett.84.6078
108. S. Das, H.-Y. Chen, A.V. Penumatcha, J. Appenzeller, High performance multilayer MoS_2 transistors with scandium contacts. Nano Lett. **13**(1), 100 (2013). https://doi.org/10.1021/nl303583v
109. Z. Yang, C. Kim, K.Y. Lee, M. Lee, S. Appalakondaiah, C. Ra, K. Watanabe, T. Taniguchi, K. Cho, E. Hwang, J. Hone, W.J. Yoo, A fermi-level-pinning-free 1D electrical contact at the intrinsic 2D MoS_2–metal junction. Adv. Mater. **31**(25), 1808231 (2019). https://doi.org/10.1002/adma.201808231
110. G.V. Hansson, R.I.G. Uhrberg, Photoelectron spectroscopy of surface states on semiconductor surfaces. Surf. Sci. Rep. **9**(5–6), 197 (1988). https://doi.org/10.1016/0167-5729(88)90003-9
111. K. Horn, Semiconductor interface studies using core and valence level photoemission. Appl. Phys. A Solids Surf. **51**(4), 289 (1990). https://doi.org/10.1007/BF00324309
112. P. V. Galiy, M. Randle, A. Lipatov, L. Wang, S. Gilbert, N. Vorobeva, A. Kumar, C.-P. Kwan, J. Nathawat, B. Barut, S. Yin, N. Arabchigavkani, T. M. Nenchuk, T. Komesu, K. He, A. Yost, U. Singisetti, W.-N. Mei, A. Sinitskii, J. P. Bird, P. A. Dowben, in *2019 IEEE 2nd Ukraine Conference on Electrical and Computer Engineering* (IEEE, 2019), pp. 679–682. https://doi.org/10.1109/UKRCON.2019.8879963
113. S.R. McHale, J.W. McClory, J.C. Petrosky, J. Wu, A. Rivera, R. Palai, Y.B. Losovyj, P.A. Dowben, Schottky barrier formation at the Au to rare earth doped GaN thin film interface. Eur. Phys. J. Appl. Phys. **55**(3), 31301 (2011). https://doi.org/10.1051/epjap/2011110082
114 C.I. Wu, Investigation of the chemistry and electronic properties of metal/gallium nitride interfaces. J. Vac. Sci. Technol. B Microelectron. Nanom. Struct. **16**(4), 2218 (1998). https://doi.org/10.1116/1.590151
115. A. Barinov, L. Casalis, L. Gregoratti, M. Kiskinova, Au/GaN interface: initial stages of formation and temperature-induced effects. Phys. Rev. B **63**(8), 085308 (2001). https://doi.org/10.1103/PhysRevB.63.085308
116. A. Barinov, L. Casalis, L. Gregoratti, M. Kiskinova, Stages of formation and thermal stability of a gold-n-GaN interface. J. Phys. D. Appl. Phys. **34**(3), 279 (2001). https://doi.org/10.1088/0022-3727/34/3/305
117. M.-H. Kim, S.-N. Lee, C. Huh, S.Y. Park, J.Y. Han, J.M. Seo, S.-J. Park, Interfacial reaction and Fermi level movement induced by sequentially deposited metals on GaN: Au/Ni/GaN. Phys. Rev. B **61**(16), 10966 (2000). https://doi.org/10.1103/PhysRevB.61.10966
118. G. Le Lay, D. Mao, A. Kahn, Y. Hwu, G. Margaritondo, High-resolution synchrotron-radiation core-level spectroscopy of decapped GaAs(100) surfaces. Phys. Rev. B **43**(17), 14301 (1991). https://doi.org/10.1103/PhysRevB.43.14301
119. P.E.C. Franken, V. Ponec, Ethylene adsorption on thin films of Ni, Pd, Pt, Cu, Au and Al; work function measurements. Surf. Sci. **53**(1), 341 (1975). https://doi.org/10.1016/0039-6028(75)90134-X
120 T.U. Kampen, W. Mönch, Lead contacts on Si(111):H-1 × 1 surfaces. Surf. Sci. **331–333**(PART A), 490 (1995). https://doi.org/10.1016/0039-6028(95)00079-8
121. R. Schlaf, O. Lang, C. Pettenkofer, W. Jaegermann, Band lineup of layered semiconductor heterointerfaces prepared by van der Waals epitaxy: charge transfer correction term for the electron affinity rule. J. Appl. Phys. **85**(5), 2732 (1999). https://doi.org/10.1063/1.369590
122 G. Song, M.Y. Ali, M. Tao, A high Schottky-Barrier of 1.1 eV between Al and S-passivated p-type Si(100) surface. IEEE Electron Device Lett. **28**(1), 71 (2007). https://doi.org/10.1109/LED.2006.887942

© The Author(s) 2022

123. M. Fontana, T. Deppe, A.K. Boyd, M. Rinzan, A.Y. Liu, M. Paranjape, P. Barbara, Electron-hole transport and photovoltaic effect in gated MoS_2 Schottky junctions. Sci. Rep. **3**(1), 1634 (2013). https://doi.org/10.1038/srep01634
124. D.A. Svintsov, A.V. Arsenin, D.Y. Fedyanin, Full loss compensation in hybrid plasmonic waveguides under electrical pumping. Opt. Express **23**(15), 19358 (2015). https://doi.org/10.1364/OE.23.019358
125. T. Weidner, A. Shaporenko, J. Müller, M. Schmid, P. Cyganik, A. Terfort, M. Zharnikov, Effect of the bending potential on molecular arrangement in alkaneselenolate self-assembled monolayers. J. Phys. Chem. C **112**(32), 12495 (2008). https://doi.org/10.1021/jp8044077
126. M. Prato, C. Toccafondi, G. Maidecchi, V. Chaudhari, M.N.K. Harish, S. Sampath, R. Parodi, V.A. Esaulov, M. Canepa, Mercury segregation and diselenide self-assembly on gold. J. Phys. Chem. C **116**(3), 2431 (2012). https://doi.org/10.1021/jp207157m
127. J. Jia, A. Bendounan, H.M.N. Kotresh, K. Chaouchi, F. Sirotti, S. Sampath, V.A. Esaulov, Selenium adsorption on Au(111) and Ag(111) surfaces: adsorbed selenium and selenide films. J. Phys. Chem. C **117**(19), 9835 (2013). https://doi.org/10.1021/jp4007203
128. W. Gordy, W.J.O. Thomas, Electronegativities of the elements. J. Chem. Phys. **24**(2), 439 (1956). https://doi.org/10.1063/1.1742493
129. A.L. Allred, Electronegativity values from thermochemical data. J. Inorg. Nucl. Chem. **17**(3–4), 215 (1961). https://doi.org/10.1016/0022-1902(61)80142-5
130. T.S. Chou, M.L. Perlman, R.E. Watson, Electronegativity and electron binding in gold alloys. Phys. Rev. B **14**(8), 3248 (1976). https://doi.org/10.1103/PhysRevB.14.3248
131. A. Neumann, K. Christmann, T. Solomun, Binding states and structural phase transformations upon iodine adsorption on a gold (100) surface. Surf. Sci. **287–288**, 593 (1993). https://doi.org/10.1016/0039-6028(93)91034-M
132. D. Nakamura, K. Ito, M. Kubo, Covalency of metal-ligand bonds in hexahaloselenates(IV) studied by the pure quadrupole resonance of halogens. Inorg. Chem. **2**(1), 61 (1963). https://doi.org/10.1021/ic50005a018
133. F. Di Quarto, M.C. Romano, M. Santamaria, S. Piazza, C. Sunseri, A semiempirical correlation between the optical band gap of hydroxides and the electronegativity of their constituents. Russ. J. Electrochem. **36**(11), 1203 (2000). https://doi.org/10.1007/BF02757695
134 M. Todeschini, A.B. da Silva Fanta, F. Jensen, J.B. Wagner, A. Han, Influence of Ti and Cr adhesion layers on ultrathin Au films. ACS Appl. Mater. Interfaces **9**(42), 37374 (2017). https://doi.org/10.1021/acsami.7b10136
135. A.V. Penumatcha, R.B. Salazar, J. Appenzeller, Analysing black phosphorus transistors using an analytic Schottky barrier MOSFET model. Nat. Commun. **6**(1), 8948 (2015). https://doi.org/10.1038/ncomms9948
136. Y.-R. Tao, X.-C. Wu, W.-W. Xiong, Flexible visible-light photodetectors with broad photoresponse based on ZrS_3 nanobelt films. Small **10**(23), 4905 (2014). https://doi.org/10.1002/smll.201401376
137. H. Fang, S. Chuang, T.C. Chang, K. Takei, T. Takahashi, A. Javey, High-performance single layered WSe_2 p-FETs with chemically doped contacts. Nano Lett. **12**(7), 3788 (2012). https://doi.org/10.1021/nl301702r
138. H. Fang, M. Tosun, G. Seol, T.C. Chang, K. Takei, J. Guo, A. Javey, Degenerate n-doping of few-layer transition metal dichalcogenides by potassium. Nano Lett. **13**(5), 1991 (2013). https://doi.org/10.1021/nl400044m
139. W. Liu, J. Kang, D. Sarkar, Y. Khatami, D. Jena, K. Banerjee, Role of metal contacts in designing high-performance monolayer n-type WSe_2 field effect transistors. Nano Lett. **13**(5), 1983 (2013). https://doi.org/10.1021/nl304777e
140. F. Iyikanat, R.T. Senger, F.M. Peeters, H. Sahin, Quantum-transport characteristics of a p-n junction on single-layer TiS_3. ChemPhysChem **17**(23), 3985 (2016). https://doi.org/10.1002/cphc.201600751
141. Y. Saeed, A. Kachmar, M.A. Carignano, First-principles study of the transport properties in bulk and monolayer MX_3 (M = Ti, Zr, Hf and X = S, Se) compounds. J. Phys. Chem. C **121**(3), 1399 (2017). https://doi.org/10.1021/acs.jpcc.6b08067
142. J. Liu, Y. Guo, F.Q. Wang, Q. Wang, TiS_3 sheet based van der Waals heterostructures with a tunable Schottky barrier. Nanoscale **10**(2), 807 (2018). https://doi.org/10.1039/C7NR05606K
143. R. Sun, Y. Gu, G. Yang, J. Wang, X. Fang, N. Lu, B. Hua, X. Yan, Theoretical study on the interfacial properties of monolayer TiS_3–metal contacts for electronic device applications. J. Phys. Chem. C **123**(12), 7390 (2019). https://doi.org/10.1021/acs.jpcc.8b08946
144. N. Tripathi, V. Pavelyev, P. Sharma, S. Kumar, A. Rymzhina, P. Mishra, Review of titanium trisulfide (TiS_3): a novel material for next generation electronic and optical devices. Mater. Sci. Semicond. Process. **127**, 105699 (2021). https://doi.org/10.1016/j.mssp.2021.105699
145. M.M. Perera, M.-W. Lin, H.-J. Chuang, B.P. Chamlagain, C. Wang, X. Tan, M.M.-C. Cheng, D. Tománek, Z. Zhou, Improved carrier mobility in few-layer MoS_2 field-effect transistors with ionic-liquid gating. ACS Nano **7**(5), 4449 (2013). https://doi.org/10.1021/nn401053g
146. H.-J. Chuang, X. Tan, N.J. Ghimire, M.M. Perera, B. Chamlagain, M.M.-C. Cheng, J. Yan, D. Mandrus, D. Tománek, Z. Zhou, High mobility WSe_2 p - and n - type field-effect transistors contacted by highly doped graphene for low-resistance contacts. Nano Lett. **14**(6), 3594 (2014). https://doi.org/10.1021/nl501275p

Publisher's Note Springer Nature remains neutral with regard to jurisdictional claims in published maps and institutional affiliations.

© The Author(s) 2022